The Journal of the Acoustical Society of America

NOVEMBER 15 2022

Evaluation of different Maritime rapid environmental assessment procedures with a focus on acoustic performance

Paolo Oddo; Silvia Falchetti; Salvatore Viola; Giuliana Pennucci; Andrea Storto; Ines Borrione; Giacomo Giorli; Elisa Cozzani; Aniello Russo; Cristina Tollefsen

J. Acoust. Soc. Am. 152, 2962–2981 (2022)
https://doi.org/10.1121/10.0014805

ASA ACOUSTICAL SOCIETY OF AMERICA

JASA ARTICLE

Evaluation of different Maritime rapid environmental assessment procedures with a focus on acoustic performance

Paolo Oddo,[1,a),b)] Silvia Falchetti,[1] Salvatore Viola,[1,c)] Giuliana Pennucci,[1] Andrea Storto,[1,d)] Ines Borrione,[1] Giacomo Giorli,[1] Elisa Cozzani,[2] Aniello Russo,[1,4] and Cristina Tollefsen[3]

[1]*NATO Centre for Maritime Research and Experimentation, La Spezia, 19126, Italy*

[2]*Department of Physics and Astronomy, University of Bologna, Bologna 40127, Italy*

[3]*Defence Research and Development Canada, Atlantic Research Centre, Dartmouth, Nova Scotia B2Y 3G8, Canada*

[4]*DISVA, Universita' Politecnica delle Marche, Ancona 60131, Italy*

ABSTRACT:

Four different Marine Rapid Environmental Assessment (MREA) procedures are compared with a focus on underwater acoustic performance. Co-located oceanographic-acoustic data were collected during the summer of 2015 in the Northwestern Mediterranean in the framework of a sea trial led by the NATO Centre for Maritime Research and Experimentation. The data were used to link MREA procedures and ocean-acoustic validation in a seamless framework. The MREA procedures consider Conductivity Temperature Depth (CTD) data, operational products from the Copernicus Marine Service, and two dynamical downscaling systems (with and without data assimilation). A portion of the oceanographic data are used for the assimilation procedure, and the remaining portion is withheld from the assimilation system for use as an independent verifying dataset. The accuracy of modelled acoustic properties is evaluated using the sound speed estimates from the different MREA methodologies as inputs to an acoustic model, and then comparing the modelled and observed acoustic arrival intensities and temporal structure. In 95% of the studied cases, the assimilative dynamical downscaling approach provides acoustic results equaling or exceeding in skill those modelled with the sound speed extracted from CTD casts. Acoustic assessment results indicate that our implementation of dynamical downscaling has skill at oceanographic scales of 4 km, about ten times larger than the ocean model horizontal resolution. https://doi.org/10.1121/10.0014805

(Received 2 May 2022; revised 22 July 2022; accepted 23 September 2022; published online 15 November 2022)

[Editor: Timothy Duda] Pages: 2962–2981

I. INTRODUCTION

The concept of Marine Rapid Environmental Assessment (MREA) was developed in the late 1990s as a methodology to collect marine data that is used to improve knowledge of the marine state and specific ocean dynamical processes, and increase the skill of ocean analyses and forecasts (Robinson and Sellschopp, 2002). A key aspect of MREA is to effectively respond to environmental assessment requests on short notice. An efficient data production-dissemination cycle may be more important than achieving the highest possible quality (Hagen *et al.*, 2008). Thus, the success of any MREA activity relies on the optimization of the full operational chain: data acquisition, data processing (including assimilation in ocean models), data integration, and their dissemination with all stakeholders. To meet these requirements, an efficient organization structure is required, which relies on efficient computing resources, and data communication channels. Adopted solutions clearly depend on the specific MREA exercise. In general, sub-sampling is a common approach used in real-time oceanographic data transfer while dedicated transfer protocols have been developed to support the exchange of large model results transfer (Signell *et al.*, 2008).

Monitoring programs that continuously collect oceanographic and geophysical data are reaching a level of maturity capable of offering a reliable source of global data (Legler *et al.*, 2015; Le Traon *et al.*, 2015). Observational data are often available to the stakeholders and are also ingested in operational ocean models, with global or regional coverage, delivering different kinds of products to a wide range of users in temporal frames compatible with most of the MREA applications. Additional and complementary data are often provided by dedicated environmental/geophysical surveys in the area of interest. However, although for many applications the available information might already be sufficient, in a full fit-for-purpose perspective, the requirements in terms of accuracy and spatial or temporal resolution depend on the specific use. Thus, there are several applications where weaknesses still exist due to the limited spatial and temporal coverage of the data. To fill the observational gaps and produce consistent estimates of the environmental state and its temporal evolution, ad-hoc ocean observing and prediction systems—integrating observations

[a)]Electronic mail: paolo.oddo@unibo.it

[b)]Current address: Department of Physics and Astronomy, University of Bologna, Bologna 40127, Italy.

[c)]Current address: Istituto Nazionale di Fisica Nucleare-Laboratori Nazionali del Sud, Catania, 95123, Italy.

[d)]Current address: Consiglio Nazionale delle Ricerche, Istituto di Science Marine, Rome, 00133, Italy.

https://doi.org/10.1121/10.0014805

through assimilative ocean numerical models—are often used with the MREA methodology. All applications involving acoustic propagation, like sonar performance prediction, are particularly relevant in a military scenario and are very sensitive to the ocean properties in which the sound propagates (Etter, 2012). Different environmental characteristics, such as the properties of the sea surface, the water column structure, and the sea floor composition and shape, all contribute to sound propagation dynamics. However, assessing the quality of an ocean estimate (hindcast, nowcast, or forecast) in terms of acoustic performance is a difficult exercise because of the scarcity of available acoustic observations and the lack of well-established validation procedures and skill score metrics. In the present study, four different MREA procedures are compared, complementing standard oceanographic data with acoustic observations. The objective of this study is to validate and assess state-of-the-art algorithms in high resolution assimilative ocean modelling used to characterize and predict the marine environment, with the aim of supporting applications based on underwater acoustic propagation.

Considering that a second-order numerical scheme requires about ten grid points to represent properly a first derivative for a given wavelength (Roache, 1998), the physics explicitly resolved in the model has scales approximately 10 times larger than the model horizontal resolution. To resolve oceanographic scales on the order of a few kilometers needed for most acoustic applications, a horizontal resolution of a few hundred meters should be used, at the price of increased computational cost. However, with present computing capabilities, operational centers are only able to provide global or regional products with model resolution of a few kilometers. In addition, when explicitly resolving small scale ocean dynamics, data assimilation and observational strategy must be adapted accordingly so that numerical uncertainties do not dominate the solution (Jacobs *et al.*, 2021).

This study exploits a quasi-synoptic oceanographic and acoustic dataset collected in the Ligurian Sea (Northwestern Mediterranean Sea) with autonomous platforms and moored sensors during the Glider Sensors and Payloads for Tactical Characterization of the Environment 2015 (GLISTEN-15) sea trial led by the NATO Centre for Maritime Research and Experimentation (CMRE). MREA acoustic properties and performance are evaluated *via* numerical experiments performed using a ray-tracing acoustic model that is forced with a variety of different sound speed estimates, and comparing the resulting acoustic arrival patterns with the observed ones. Given that the acoustic arrival patterns are sensitive to vertical sound speed gradients, short to medium range acoustic transmissions also provide essential information on the vertical temperature structure to inform ocean state estimates.

After the introduction in Sec. II, the experimental design employed during GLISTEN-15 is illustrated from both the observational and modelling points of view. Details are provided on the experimental geometry, the resulting dataset, the ocean and acoustic model setup and implementation, as well as the data assimilation scheme used. In Sec. III, the observed hydrographic characteristics are studied, and model results assessed from both oceanographic and acoustic viewpoints. Finally, Sec. IV presents the summary and conclusions.

II. THE EXPERIMENTAL DESIGN

A. GLISTEN-15 experiment

The GLISTEN-15 sea trial was conducted from August 26, 2015 to September 9, 2015 in the Tyrrhenian Sea, North of the Elba Island (Fig. 1). The GLISTEN-15 sea trial was one of the sea- going experimental efforts at CMRE with a special emphasis on acoustic remote sensing using underwater glider platforms. The main objective of GLISTEN-15 was to evaluate the benefits of *in situ* measurements of

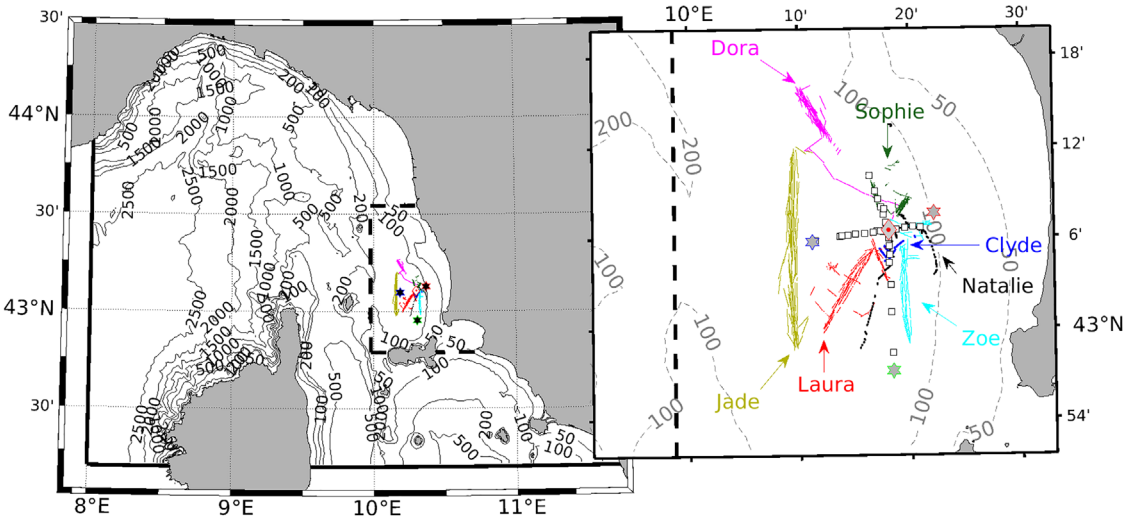

FIG. 1. (Color online) Area of the GLISTEN-15 sea trial and numerical experiment. In the left panel, the model domains and bathymetry (m) are shown, the solid black lines indicate the boundaries of the parent model, and the dashed lines indicate the boundaries of the nested models. The right panel is an enlargement of the experimental area. Colored lines indicate the gliders' trajectory. Small white squares indicate the position of the acoustic and CTD stations. A white diamond with red edges indicates the position of the SLIVA buoy. Grey hexagrams with green, blue, and red edges indicate the position of oceanographic moorings 1, 2, and 3, respectively.

relevant environmental variables and parameters for sonar performance prediction. However, given the large amount of data collected, GLISTEN-15 also provided the opportunity for complementary ocean-acoustic studies. In particular, the synoptic ocean-acoustic observations collected using gliders and fixed platforms allows us to study and characterize the performance of four different MREA procedures targeted to underwater acoustic applications. More generally, the MREA procedures can also be evaluated from an acoustic point of view.

The NATO Research Vessel (NRV) Alliance provided logistic and scientific support during the entire operation (Fig. 1). Seven gliders (named Dora, Zoe, Clyde, Laura, Sophie, Jade, and Nathalie) equipped with standard oceanographic sensors and various acoustic payloads were deployed during the experiment. In addition, three oceanographic moorings and one acoustic mooring equipped with a vertical line array (VLA) of hydrophones (termed Slim Line Vertical Array, SLIVA) were deployed. To study acoustic properties, two major acoustic propagation axes were considered in terms of bathymetry and were sampled by CTD casts (Fig. 1): a track parallel to the coastline and along a bathymetric isobath (115 m depth); and a second track perpendicular to the coastline crossing several bathymetric lines (100–127 m depth). The SLIVA was deployed at the crossing point of the two acoustic tracks. An acoustic source was deployed from the NRV Alliance at fixed distances from 0.5 to 15.0 km from the SLIVA (i.e., *acoustic* stations) and along the two different acoustic transects while the ship was stationary. For each acoustic station, the source was deployed at 30 and 60 m depth. The three oceanographic moorings were deployed at the east and west ends of the acoustic track perpendicular to the coastline, and at the southern end of the track parallel to the coastline (Fig. 1).

1. Available observational data

Two oceanographic gliders (Dora and Jade) were deployed from August 26, 2015 to September 9, 2015 to collect data along the northern and western boundaries of the experimental area and to provide information about the oceanographic lateral advective forcing (Fig. 1). During the same period, five additional hybrid oceanographic–acoustic gliders were deployed several times for short- to medium-term missions, coordinating their positions and trajectories with the acoustic asset towed or deployed from the ship (Fig. 1). During the experiment, all the gliders transmitted oceanographic data every 3 h. According to CMRE protocols, real-time glider data are subsampled to reduce to about 25% their volume compared to the full resolution dataset. An automatic quality control procedure is applied in real time to the glider data before being ingested into the ocean model. The data collected by the autonomous platforms were complemented with three fixed oceanographic moorings (hereafter, OM-1, OM-2, and OM-3) (Fig. 1). The three moorings were equipped with various sensors measuring temperature and salinity to monitor the high frequency ocean dynamics with particular emphasis on the near-surface layers (top 50 m). Table I reports a list of the instruments used in the GLISTEN-15 experiment. For the purposes of the present study, the acoustic dataset collected using the source deployed from the ship and the moored SLIVA receiver are used. The source was deployed from NRV Alliance at predefined stations along the two major propagation axes and held at a fixed location while a repeating set of pulses was transmitted (Fig. 1). The 6 s transmission sequence consisted of 6 continuous wavelength (CW) 1 s pulses transmitted simultaneously; 2 s of silence; a single 1 s linear frequency modulated (LFM) (875–5000 Hz) chirp; and 2 s of silence. The duration of each transmission period was typically 5 min, and the transmission sequence was performed twice at each station: once with the source deployed at 60 m depth, and again with the source deployed at 30 m depth. The SLIVA array consists of 32 omnidirectional hydrophones spaced by 1.5 m and recording at a sample rate of 19531.25 Hz. The array was also equipped with three pressure sensors for accurate estimate of the depth of the hydrophones at the time of each transmission. The depth of the central hydrophone was on average approximately 55 m, and the top-most and bottom-most hydrophones were at depths of approximately 30 and 80 m, respectively.

Additional oceanographic data were collected using instruments deployed from the ship. In particular, 37 CTD casts were collected at the location of the acoustic transmissions immediately before the activation of the sound source. The total collected dataset was split into two sets: a sub-set

TABLE I. Summary of the available oceanographic and acoustic data.

Instrument/platform	n	From	To	Additional details
Oceanographic gliders	2	August 26	September 9	Dora and Jade. T and S data. (Assimilated)
Ocean/Acoustic gliders	6	August 18	September 9	Laura, Natalie, Sophie, Zoe a,nd Clyde. T,S and acoustic
Oceanographic moorings	3	August 26	September 8	Named OM1, OM2, and OM3. T and S data.
CTDs	37	August 28	September 8	Deployed from the NRV Alliance. T and S data.
SLIVA (VLA)	1	August 28	September 7	Vertical line array (32 channels). Acoustic pressure data. Sample rate of 19531.25 Hz.
Acoustic source	1	August 28	September 7	28 stations with 5 min signal pattern: [0–1 s] CW 331,419,509,863,1109,1433 Hz [1–3 s] Null/Silence [3–4 s] LFM 975-5000 (Hz) [5–6 s] Null/Silence

https://doi.org/10.1121/10.0014805

of oceanographic data from gliders was assimilated in the ocean model while all the observations from the remaining gliders and moorings, both oceanographic and acoustic, were used only for model validations purposes. The two gliders selected for the assimilation process, Jade and Dora, were deployed and performed their mission outside the study area near the western and northern boundaries of the experiment (Fig. 1), thus, only remotely constraining the model solution.

B. Numerical Experiments

1. Ocean model

The analysis system implemented for the experiments is based on the Nucleus for European Modelling of the Ocean (NEMO) primitive equation model, version 4.0.4 (Madec and the NEMO team, 2012) and built upon previous modelling experience at CMRE (Oddo *et al.*, 2016). The modelling suite makes use of two models (hereafter called parent and child) and the two-way nesting algorithm to reach the appropriate horizontal resolution in the experimental area. The two-way nesting is implemented using the adaptive grid refinement in Fortran (AGRIF) (Debreu *et al.*, 2008). The interaction between grids is "two-way" in the sense that the parent grid feeds the open boundaries of the child grid, while the child grid provides volume averages of prognostic variables to the parent grid once a given number of time steps is completed. The NEMO parent domain covers the entire Ligurian Sea with two lateral open boundaries on the western and southern sides located at 8.0 E and 42.2 N, respectively, while the child domain focuses on the GLISTEN-15 area (Fig. 1). The modelling system is thus configured such that the parent model constrains the large-scale and the child model focusses on the experiment area.

The bathymetry is taken from the General Bathymetric Chart of the Oceans (GEBCO) (Weatherall *et al.*, 2015). The horizontal resolution of the parent model is about 1.125 and 1.5 km along the zonal and meridional directions, respectively, while the nested domain corresponding resolution reaches 375 and 500 m. Both domains share the same vertical grid, which is discretized using 141 depth levels with partial steps (Barnier *et al.*, 2006). Surface fluxes are calculated by using the bulk formulas of Pettenuzzo *et al.* (2010). The input atmospheric fields (i.e., air temperature, humidity, winds and cloud cover) for the bulk formulas are taken from the European Centre for Medium Range Weather Forecast (ECMWF) operational analyses at a three-hourly frequency.

The NEMO parent model is initialized and one-way nested with the Copernicus Marine Service (CMEMS) (Le Traon *et al.*, 2019) Mediterranean Sea operational model (Oddo *et al.*, 2014) which has a horizontal resolution approximately of 4.5 and 3.5 km along the meridional and zonal directions. The one-way nesting procedure uses a Flather (Flather, 1976) formula for the barotropic velocities, a flow relaxation scheme for the baroclinic velocities, and a radiation scheme for active tracers (Oddo and Pinardi, 2008). The model uses a split-time step technique to resolve, in a computationally efficient way, the slow and fast ocean dynamics. The baroclinic model time step is 150 s in the parent grid and 50 s in the child, and 40 and 20 sub-loops are performed to resolve the barotropic component in the parent and child model, respectively. In both models (parent and child), for the active tracers (temperature and salinity), a 4th order Flux Correct Transport scheme was adopted (Zalesak, 1979) to resolve advection while a bi-laplacian operator along iso-neutral surfaces resolves horizontal diffusion. The momentum equation is numerically solved using a 3rd order upstream biased scheme (Shchepetkin and McWilliams, 2005) for the advective terms and a bi-laplacian operator along iso-level surfaces for the viscous terms. Horizontal diffusivity and viscosity values are homogeneous in the interior of the model domain while they are doubled approaching the coast and the lateral open boundaries starting from a distance equal to ten model grid points. This spatially varying diffusivity and viscosity scheme was implemented to preserve numerical stability while minimizing numerical dissipation. The atmospheric pressure forcing term was added to the governing equations for consistency with the CMEMS model, with pressure fields obtained from the ECMWF operational analyses and forecasts. The vertical turbulent coefficients are computed using the generic length scale turbulent closure scheme (Umlauf and Burchard, 2003, 2005).

To properly constrain the model surface temperature, the satellite level-4 Sea Surface Temperature (SST) product from CMEMS (Buongiorno Nardelli *et al.*, 2013) is ingested into the model through adjustment of the surface heat flux by means of a Newtonian relaxation algorithm. Using a flux formulation, a feedback term is added to the surface heat flux. The feedback coefficient is taken equal to $-40\,\mathrm{Wm^{-2}K^{-1}}$ at nighttime, and it gradually decreases to $0\,\mathrm{Wm^{-2}K^{-1}}$ at noon because of the use of nighttime measurements only in the production of the SST analysis. Light extinction coefficients are computed interactively using the satellite retrieved chlorophyll values (Lengaigne *et al.*, 2007).

2. Ocean Data assimilation

A three-dimensional variational (3DVAR) algorithm was used to constrain the model solution. The data assimilation was performed on the child model and the corrections were therefore propagated into the parent model due to the two-way nesting procedure. The 3DVAR formulation was chosen because it is relatively easy to implement and to expand, it can easily take into consideration different estimates of background error covariance matrix, its core is independent of the primitive equations model core, and it is portable.

The cost function in 3DVAR is defined as

$$J(\boldsymbol{x}) = \frac{1}{2}(\boldsymbol{x}-\boldsymbol{x}_b)^T\mathbf{B}^{-1}(\boldsymbol{x}-\boldsymbol{x}_b) + \frac{1}{2}(\boldsymbol{y}-H[\boldsymbol{x}])^T\mathbf{R}^{-1}(\boldsymbol{y}-H[\boldsymbol{x}]), \quad (1)$$

where $\boldsymbol{x}$ is the analysis state vector at the minimum of J, $\boldsymbol{x_b}$ is the background state vector, $\mathbf{B}$ is the background error covariance matrix, H is the non-linear observational operator, $\boldsymbol{y}$ are the observations, $\mathbf{R}$ is the observational error covariance matrix, and T indicates the matrix transpose. Following Dobricic and Pinardi (2008), the adopted 3DVAR scheme assumes that the $\mathbf{B}$ matrix can be rewritten and thus, decomposed as follows:

$$\mathbf{B} = \mathbf{V}\mathbf{V}^{\mathrm{T}}, \tag{2}$$

$$\mathbf{V} = \mathbf{V}_{\mathrm{D}}\mathbf{V}_{\mathrm{u,v}}\mathbf{V}_{\eta}\mathbf{V}_{\mathrm{H}}\mathbf{V}_{\mathrm{V}}. \tag{3}$$

This also has the advantage of imposing a pre-conditioning, as the minimization is performed on the control variable $\boldsymbol{v}$ (with $\delta\boldsymbol{x}=\mathbf{V}\boldsymbol{v}$), which also serves the purpose of avoiding the inversion of $\mathbf{B}$.

The background error covariance matrix $\mathbf{B}$ is modelled as a linear sequence of several $\mathbf{V}$ operators. Each operator in which $\mathbf{V}$ is decomposed defines a specific error space. From right to left, $\mathbf{V}_{\mathrm{v}}$ defines the vertical covariance, $\mathbf{V}_{\mathrm{H}}$ projects the vertical increments onto the horizontal space by means of a recursive filter, $\mathbf{V}_{\eta}$ (the balance operator) is a two-dimensional barotropic model accounting for sea surface height adjustments, and $\mathbf{V}_{\mathrm{u,v}}$ forces a geostrophic balance between temperature, salinity, and the velocity components. Finally, $\mathbf{V}_{\mathrm{D}}$ is a divergence-damping operator avoiding spurious currents close to the coast in the presence of complex coastlines (details in Dobricic and Pinardi, 2008). In our formulation of the 3DVAR, the vertical transformation operator $\mathbf{V}_{\mathrm{v}}$ has the form

$$\mathbf{V}_{\mathrm{V}} = \mathbf{S}_{\mathbf{c}}\boldsymbol{\Lambda}_{\mathbf{c}}{}^{1/2}, \tag{4}$$

where columns of $\mathbf{S}_{\mathbf{c}}$ contain multivariate eigenvectors and $\boldsymbol{\Lambda}_{\mathbf{c}}$ is a diagonal matrix with eigenvalues of empirical orthogonal functions (EOFs). In the present study, a set of EOFs was calculated from an ensemble of model simulations obtained, perturbing a few model parameters and the initial conditions. The EOFs were computed by dividing the whole area covered by the child domain into three sub-regions to account for the different error dynamics. For each sub-region, a set of 40 tri-variate (temperature, salinity, and sea surface height) EOFs was computed by removing the temporal trend and normalizing the anomalies using a depth dependent standard deviation. To ensure ergodicity within each region, data were subsampled horizontally every five grid points, and temporally sampled every 2nd day from July 6 to September 6. In Fig. 2, the regions and the first four temperature and salinity EOFs are shown for the central region.

In all three regions, the EOFs (not shown) are similar, indicating similar model error characteristics. The temperature and salinity errors are dominated by deepening of the mixed layer depth and the thermocline. It is interesting to note that the 3rd and 4th salinity EOFs are similar indicating that different errors in temperature correspond to the same error in salinity. Some variability may be also due to the intrusion of Atlantic and modified Levantine waters.

$\mathbf{V}_{\mathrm{H}}$ is the same in the three regions with horizontal correlation radii equal to 7 and 8 km along the zonal and meridional directions, respectively. The diagonal observational error covariance matrix, $\mathbf{R}$, which accounts for instrumental and representation errors, is assumed to have no spatial or temporal variability and was shaped along the vertical dimension to resemble the non-assimilated glider-measured full standard deviation.

3. Acoustic model

The acoustic model used in this study is based on Bellhop (Porter and Bucker, 1987; Porter and Liu, 1994) which is a highly efficient beam tracing model used to predict acoustic pressure fields in ocean environments. The

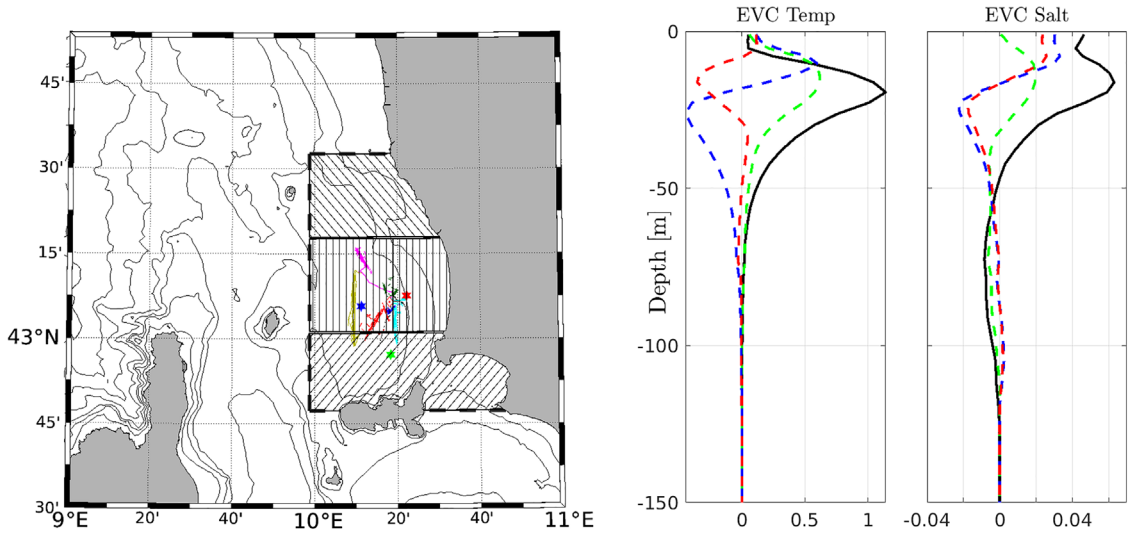

FIG. 2. (Color online) Left panel: Regions in the parent model where different sets of EOFs were computed. The right panels show the first four eigenvectors (EVC) for temperature and salinity for the central region, where most of the data were collected, scaled by the corresponding eigenvalues (bold black, dashed green, blue, and red for the first, second, third, and fourth EVC, respectively).

https://doi.org/10.1121/10.0014805

beam tracing structure leads to a particularly simple and flexible algorithm (Jensen *et al.*, 1994). The model was implemented with a range-dependent bottom boundary and sound speed profile while the ocean surface is modelled as a vacuum. Bottom depth is from GEBCO, and the sound speed profiles are interpolated into the acoustic model grid using a bi-linear interpolation. The simulated sound source frequency was 3100 Hz, the highest frequency clearly detectable at the longest ranges studied. While the sea-bottom depth varies with range, the sea-bottom acoustic properties were assumed to be constant along the modelled acoustic sections. Basic properties of the sea bottom are based on previous modelling studies on the same area (Tollefsen, 2021). The bottom is modelled as an acousto half-space with sound speed of 1551 ms^{-1}, density equal to 1.6 g cm^{-3}, and a bottom attenuation equal to 0.15 dB λ^{-1}. Differently from Tollefsen (2021), we omitted the low sound-speed layer overlying the half-space because only the very short range stations could have been affected by this parameterization. Several types of beams are implemented in Bellhop (Porter and Bucker, 1987; Jensen *et al.*, 1994; Porter and Liu, 1994). In the present study, we used Gaussian beam bundles (Weinberg and Keenan, 1996). Finally, incoherent transmission loss calculations were used to filter out small random differences in the sound speed profiles provided by the three ocean model simulations.

4. Numerical experiment setup

Two experiments were performed with the ocean modelling suite described. The simple dynamical downscaling (Exp-DD) with no data assimilation was initialized on June 6, 2015 from the available operational CMEMS products in the area and run until September 9, 2015. The model was initialized approximately 3 months before the start of the GLISTEN-15 experiment to let the ocean dynamics, resolved by the increased model resolution, properly develop. A second experiment with data assimilation (Exp-DA) was initialized, at the beginning of the GLISTEN-15 experiment on August 26 from Exp-DD. Daily assimilation cycles were performed until September 9, and innovations were calculated using the First Guess at Appropriate Time (FGAT) method. The goal is to understand whether the MREA procedure would benefit from gliders diving in proximity of the area of interest (far enough away to prevent interfering with the operations); therefore, in Exp-DA, only data from the Jade and Dora gliders (Fig. 2) were assimilated. All the other data (gliders, moorings, and CTDs) were used only for model validation purposes.

A total of 53 acoustic model configurations were implemented. They correspond to 27 stations where the fixed-source fixed receiver experiments were carried out with the acoustic source deployed at 60 m depth, and 26 stations with the source deployed at 30 m depth (Table I and Fig. 1). In each configuration, the acoustic modeling was performed for four environmental characterizations: using range independent sound speed measured by the CTD casts synoptic with the acoustic transmission, and using range dependent sound speed estimates deriving from the three model based MREA methodologies (CMEMS, Exp-DD, and Exp-DA). In the case of CTD-derived sound speed profiles, the measured profiles were assumed constant for the entire sound propagation path (i.e., the acoustic model had range-dependent bathymetry with a range-independent sound speed profile). In the other acoustic configurations, the sound speed estimates varied along the acoustic propagation path, and were obtained by bi-linear interpolation of the corresponding ocean model results. To investigate the impact on the acoustic model estimates of the sound speed spatial variability along the propagation path, additional acoustic experiments were carried out using average sound speed estimates from the model results. Sound speed predicted by CMEMS, Exp-DD, and Exp-DA were averaged along the propagation path and used as input for the acoustic model and (as with the simulation performed using the CTD-measured sound speed profile), the acoustic model was run with range-dependent bathymetry and a range-independent sound speed profile. Table II summarizes the numerical experiments. Overall, the adopted modelling strategy fits well with the MREA requirements. In our workstation, the two-way nested system requires approximately 15 min to simulate one day; the data-assimilation in average converged in 5 min, while individual acoustic model simulations an additional 5 min. As a result, in an operational framework, with the presented procedure, and accounting also for data transfer, the modelling framework could provide an environmental assessment about 1 h after the beginning of the glider data transfer procedure.

III. RESULTS

A. Observed hydrographic conditions during GLISTEN-15

The study of the oceanographic characteristics and water properties of the area during the experiment starts from the analysis of the CTD data (Fig. 3). Most of the

TABLE II. Ocean and acoustic model experiments.

Ocean model runs				
	Start date	End date	Initial conditions	Assimilated data
Exp-DD	June 6	September 9	CMEMS	None
Exp-DA	August 26	September 9	Exp-DD	Jade and Dora gliders

Acoustic model runs			
	Transects (n)	Sound speed profile	Source depth (m)
Aco-CTD	26 / 27	CTD	30 / 60
Aco-CMEMS	26 / 27	CMEMS	30 / 60
Aco-DD	26 / 27	Exp-DD	30 / 60
Aco-DA	26 / 27	Exp-DA	30 / 60
Aco-CMEMS-RI	26 / 27	Average (CMEMS)	30 / 60
Aco-DD-RI	26 / 27	Average (Exp-DD)	30 / 60
Aco-DA-RI	26 / 27	Average (Exp-DA)	30 / 60

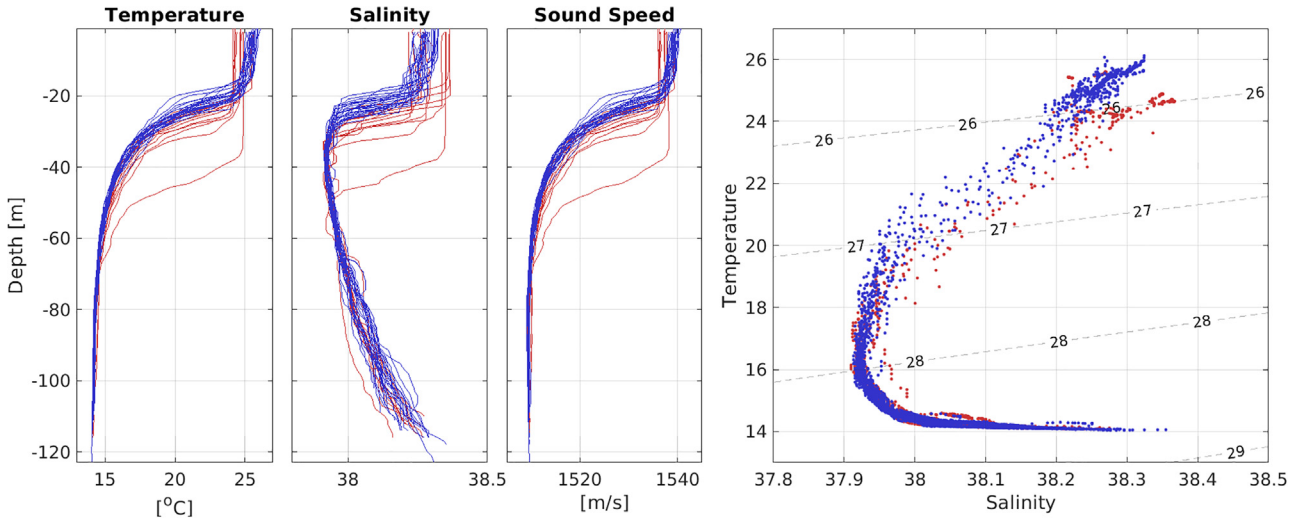

FIG. 3. (Color online) Potential temperature (°C), salinity, and sound speed (ms^{-1}) vertical CTD profiles and potential temperature-salinity diagram. Sampling positions are shown in Fig. 1. Blue lines (dots) indicate data collected before September 4, red lines (dots) indicate data collected starting from September 4.

temporal and spatial variability of temperature is confined to the mixed layer, in its thickness (i.e., the mixed layer depth, MLD), and in the depth and thickness of the thermocline. MLD varies between ∼18 and 30 m; however, a MLD of about 40 m was recorded by one CTD cast. Surface temperatures recorded during GLISTEN-15 reach values greater than 25 °C. The seasonal thermocline is quite sharp down to 50–60 m, where temperatures reach about 13–14 °C and do not vary substantially in the deeper layer. In the thermocline (halocline) layer, a salinity minimum associated with the Modified Atlantic Water (MAW) is present. Salinity variability is minimum at around 40 m suggesting that the MAW has mostly constant properties in the observational area and during the studied period. A comparison (not shown) with historical data (Coriolis, Szekely *et al.*, 2019 and World Ocean Database, Boyer *et al.*, 2018) in the area during August–September is consistent with the warming and salinification processes ongoing in the Mediterranean Sea during the last decades (e.g., Schroeder *et al.*, 2017).

Preliminary analysis of data recorded by the three ocean moorings suggests that ocean dynamics in the coastal zone, where the OM3 mooring is located, are different from those observed on OM1 and OM2, thus also explaining why some CTD profiles differ significantly from the others (Fig. 3). To better understand the temporal and spatial variability during the period of the experiment, daily data were grouped and compared. Analysis of the data in short time intervals is important considering that coastal areas are generally characterized by significant mesoscale and sub-mesoscale variability, which may evolve with time scales of very few days or even hours in the case of significant sub-mesoscale activities. Examples of such processes have already been described in the same area of the Ligurian Sea (Borrione *et al.*, 2019). The availability of diverse sampling platforms, including moving gliders, permits good coverage of the area of interest, especially on three specific dates: August 30, September 4, and September 7 (Figs. 2 and 5); therefore, allowing for an improved understanding of the oceanographic situation and its evolution.

Temperature and salinity profiles collected by all the platforms on August 30, September 4, and September 7 are shown in Fig. 4, while Fig. 5 contains temperature and

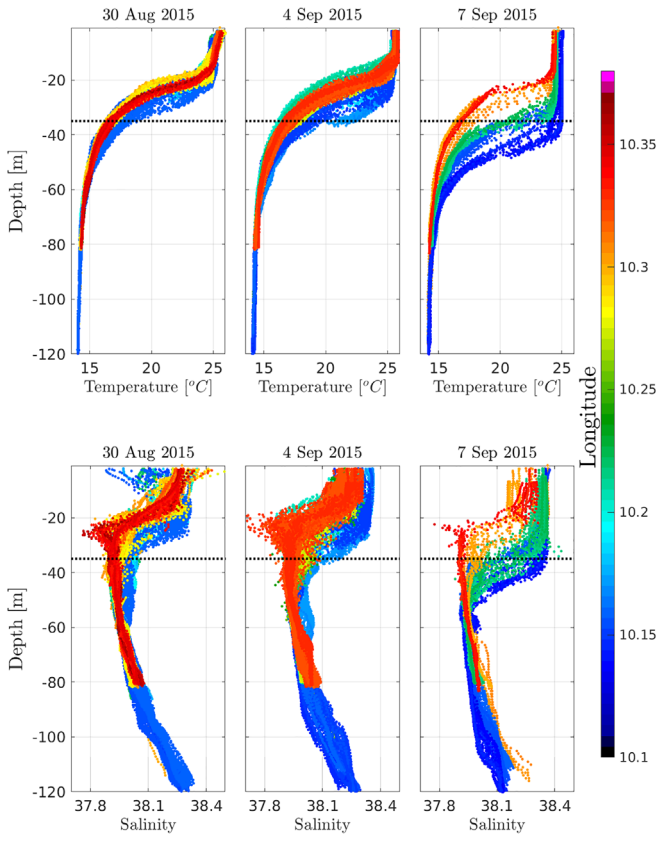

FIG. 4. (Color online) Daily (24 h) temperature (top) and salinity (bottom) profiles collected by all available sampling platforms (CTD, gliders, and moorings) during three selected dates. Color indicates the longitude of sampling. The horizontal dashed line indicates depth of 35 m used for the objective analysis in Fig. 5.

https://doi.org/10.1121/10.0014805

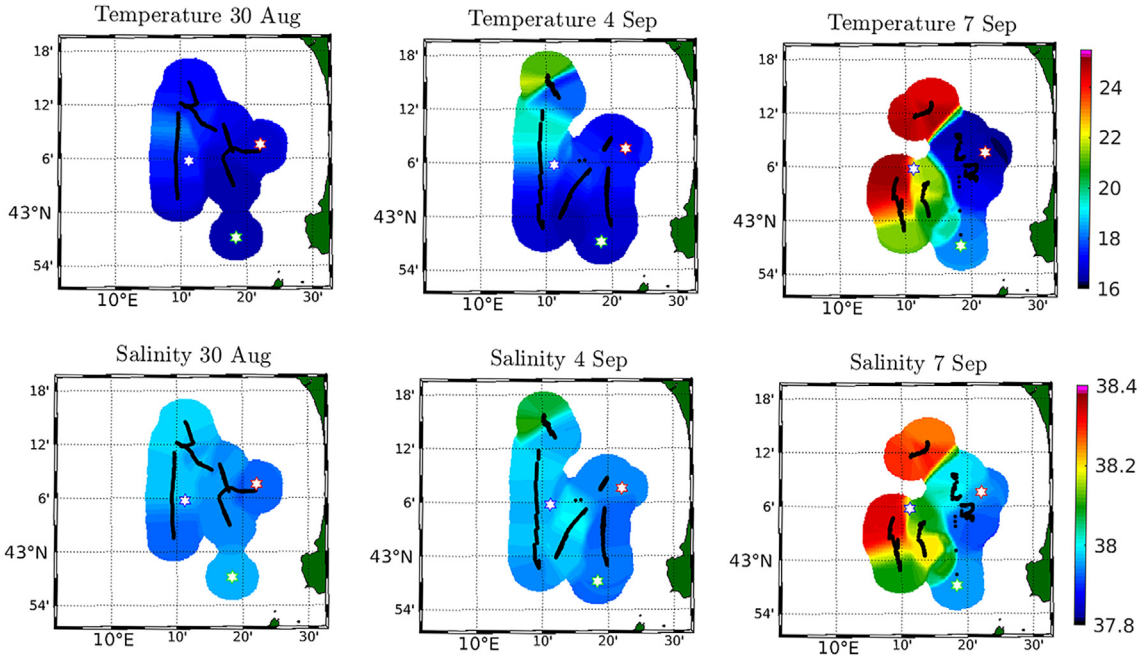

FIG. 5. (Color online) Daily objective analysis of temperature (°C, top row) and salinity (bottom row) measurements collected at 35 m depth by all available sampling platforms (CTDs, gliders, and moorings) during three selected dates: August 30, September 4, and September 7.

salinity maps at 35 m depth for those same dates, obtained through an objective analysis (OA) interpolation (Gandin, 1963) and shown together with their sampling positions. On August 30, both temperature and salinity indicate a water column structure that is similar throughout the whole sampling region (Fig. 4). The spatial uniformity is confirmed not only by the fact that longitudinal variations do not explain the small variability observed close to the surface in salinity, and at the base of the thermocline in temperature, but also by the weak horizontal variability depicted at the depth of 35 m in Fig. 5. At 35 m depth (Figs. 4 and 5), temperature and salinity on August 30 and September 4 are relatively low as a consequence of the relatively shallow MLD reaching 20 m. Differences in oceanographic conditions increase on September 4 and 7, when there is increasing spread in the observed temperature and salinity values, particularly at depths between 10 and 40 m. There appears to be a progressive intrusion of warmer and fresher water from the northwest that is more clearly seen in the OA interpolated values of Fig. 5. At the end of the sampling period (September 7), a large temperature increase and associated spatial variability is observed, especially in the north-western area of the domain (Fig. 5).

The observed increase in spatial variability is due to the presence of two distinct water masses. At depths between 25 and 40 m, the first water mass is characterized by temperatures lower than 20 °C and salinities lower than 38.18. The second water mass present in the area is characterized by temperature reaching 24 °C and salinity close to 38.3. Despite the short time interval considered, remarkable variability can be seen, mostly driven by the surface and advective fluxes. A significant increase in wind intensity (not shown) coming from west/north-west is observed on September 5, potentially driving the advection of water masses from the north with different characteristics into the region. Overall, spatial and temporal scales of the observed variability in this region are similar to those previously observed locally and in other areas of the Mediterranean Sea (Bosse *et al.*, 2015; Lermusiaux and Robinson, 2001; Robinson and Golnaraghi, 1994).

B. Ocean model results and assessment

To quantitatively assess the quality of the three different model estimates and the statistical differences between them, the modelled and observed fields are compared at the observation locations (Fig. 1). It should be noted that CMEMS data for the study period are available as daily means and thus, the diurnal variability is filtered out from the operational products. To fully assess the performance of each experiment and of the available CMEMS products, the mean squared error (e.g., Murphy, 1992) is decomposed following Oke *et al.* (2002) and the single components analyzed:

$$MSE = \frac{1}{n}\sum_{i=1}^{n}(m_i - o_i)^2 = MB^2 + SDE^2 + 2\sigma_m\sigma_o(1 - CC), \quad (5)$$

$$MB = \overline{m} - \overline{o}, \quad (6)$$

$$SDE = \sigma_m - \sigma_o, \quad (7)$$

$$CC = \frac{1}{\sigma_o}\frac{1}{\sigma_m}\frac{1}{N}\sum_{i=1}^{N}(m_i - \overline{m})(o_i - \overline{o}), \quad (8)$$

where MB is the mean bias error, SDE is the standard deviation error, and CC is the cross correlation between the

modelled and observed fields. The *i-th* modelled and observed variable is denoted by m_i and o_i, respectively; $\overline{m}$ and $\overline{o}$ are the respective means (horizontal and temporal); while σ_m and σ_o are the respective standard deviations. In addition, the unbiased root mean squared error (uRMSE), or standard deviation of the misfits, is also computed:

$$uRMSE = \sqrt{\frac{1}{N}\sum_{i=1}^{N}\left[(m_i - \overline{m}) - (o_i - \overline{o})\right]^2}. \quad (9)$$

The statistics MB, SDE, CC, and uRMSE for temperature and salinity are plotted in Fig. 6. With the exception of the CMEMS data, averaged observed and modelled temperature profiles are in good agreement. The MB temperature profiles show a weaker thermocline in CMEMS, with temperatures higher than observations between 30 and 80 m depth. Exp-DA and CMEMS have both very small MB error values from the surface down to 20 m depth, while Exp-DD slightly underestimates the near surface temperature. In the upper portion of the thermocline, Exp-DD and Exp-DA perform similarly, while from 40 m down to the bottom, the data assimilation procedure significantly improves the modelled temperature. At approximately 80 m depth, the temperature MB errors from CMEMS and Exp-DD are comparable,

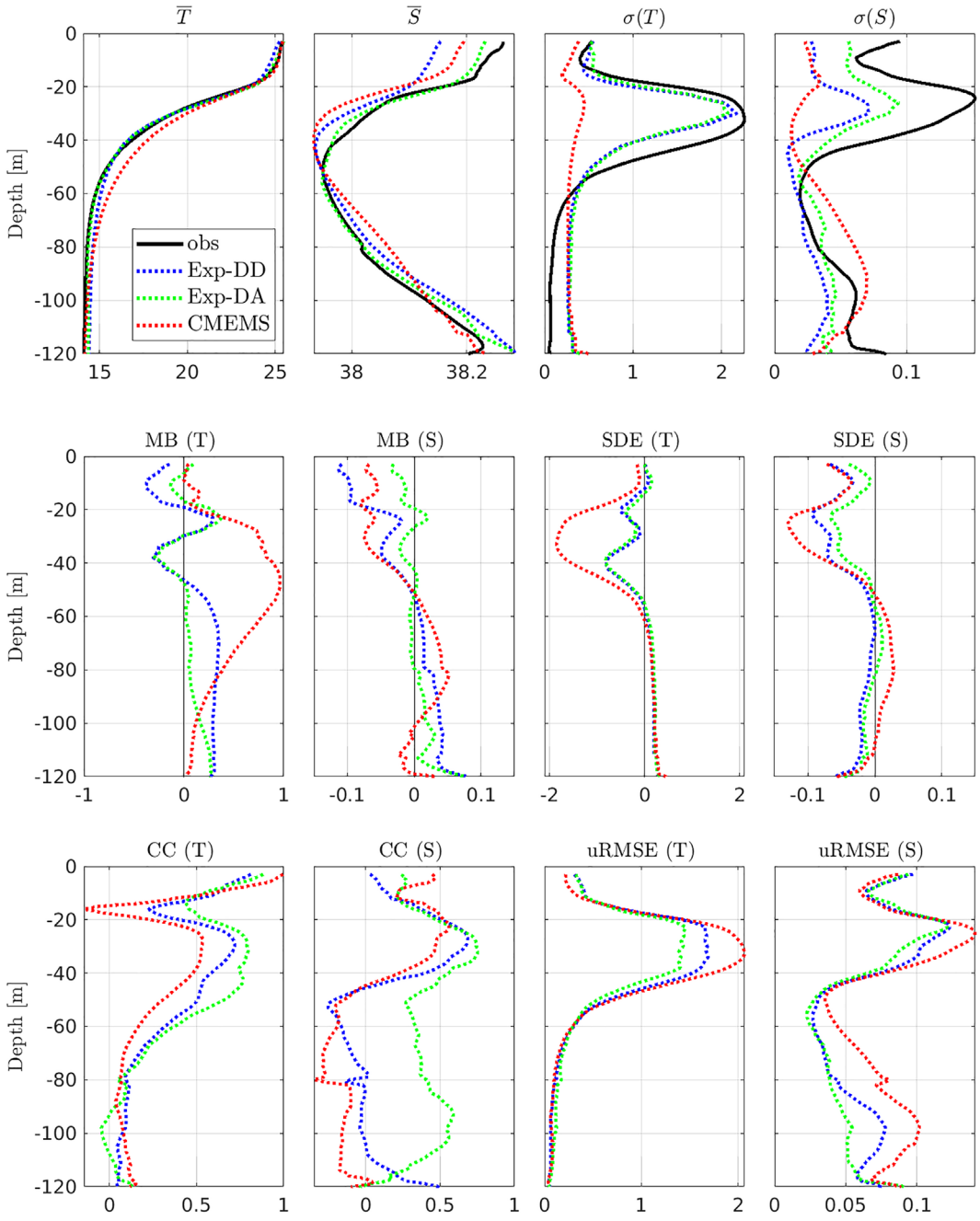

FIG. 6. (Color online) Top row, from left to right: Average temperature (°C) and salinity, temperature (°C) and salinity standard deviation. Middle panels, from left to right: temperature (°C) and salinity MB errors, temperature (°C) and salinity SDE. Bottom panel, from left to right: temperature and salinity CC, temperature and salinity uRMSE.

https://doi.org/10.1121/10.0014805

while at depths greater than 100 m, CMEMS outperforms Exp-DA. In terms of temperature standard deviation (spatial/temporal variability), the observations are characterized by a maximum at 35 m depth, probably driven by the deepening of the MLD and the advective processes previously discussed (Sec. III A).

Both Exp-DD and Exp-DA effectively reproduce the observed standard deviation in the upper 60 m despite a tendency to slightly underestimate the thickness of the layer due to the large variability. The CMEMS model underestimates the observed temperature standard deviation in the top 60 m probably due to the use of daily averages as well as the 4 km horizontal resolution which is inadequate for the resolution of small scales involved in this analysis.

All the models tend to overestimate the temperature standard deviation below 60 m depth. Temperature CC and uRMSE highlight the differences between Exp-DD and Exp-DA. These two statistical quantities account for the temperature spatial and temporal distribution. Both the downscaling and the data assimilation significantly improve the temperature estimates, due to the ability of the model to properly resolve the dominant ocean scales (Exp-DD and Exp-DA) and to accurately constrain the model solution spatially and temporally (Exp-DA). All the models succeed in reproducing the observed salinity minimum at 50 m depth where the modified Atlantic waters were observed. Except for Exp-DA, which has a quite uniform MB vertical profile, the other two models tend to underestimate the salinity values in the surface layers and overestimate the salinity in the bottom layers. The data assimilation procedure also significantly improves the salinity standard deviation. Both Exp-DD and Exp-DA properly reproduce the vertical shape of the salinity standard deviation despite modelled values that are generally smaller than the observed values. CMEMS products strongly underestimate observed salinity variability in the surface layers and overestimate it between 60 and 100 m depth.

Exp-DD and CMEMS have similar values of salinity CC with a maximum at about 35 m depth indicating accurate representation of the modified Atlantic water dynamics. Exp-DA outperforms CMEMS and Exp-DD in terms of salinity CC, especially below the halocline, where CMEMS and Exp-DD do not show statistically significant correlation with the observations. The salinity uRMSE values confirm the significant improvement in resulting from the dedicated modelling exercise, with CMEMS performing significantly worse than Exp-DD and Exp-DA.

Overall, the dynamical downscaling (with or without data assimilation) has significant impact on the model ability to correctly reproduce the observed vertical stratification and the spatiotemporal variability. The data assimilation further improves the results, mostly in terms of salinity bias and variability, but also in the upper thermocline temperature. Improvements in the near-surface layers may be particularly relevant for acoustic propagation as for mid-latitudes, and especially in the summer season, differences between MLD and sonic layer depth are negligible (e.g., Helber *et al.*, 2008).

To assess the impact on acoustics, we quantitatively evaluated the performance of the three different MREA methodologies, accounting for a modelling component, in terms of sound speed vertical derivative, which is one of the most important oceanographic properties affecting acoustic propagation. We computed the MB, SDE, CC, and uRMSE between non-assimilated glider data and different estimates of sound speed vertical derivative. Results in Fig. 7 indicate that the Exp-DD and Exp-DA estimates significantly outperform those from the available CMEMS product; however, the differences between Exp-DD and Exp-DA are relatively small outside the region corresponding to the top of the thermocline.

In terms of mean profile, all the ocean estimates can reproduce the observed minimum in sound speed gradient at 20 m depth; however, its prominence is considerably reduced in the CMEMS products. The standard deviation maximum observed at the base of the MLD is only partially reproduced in the CMEMS data while it is well captured by both Exp-DD and Exp-DA. The MB error in the three different ocean estimates has comparable values; however, in the CMEMS products, it has positive values between 20 and 40 m depth and then becomes negative toward the bottom. In the Exp-DA and Exp-DD, the MB error is negative between 20 and 40 m depth and then tends to zero in the deeper layers. Exp-DA slightly improves the representation of the sound speed profile vertical derivative mostly in terms of MB and CC in the layer between 40 and 60 m. These differences may be particularly relevant to the acoustic experiment, not only because this layer includes the thermocline, but also because it is near the acoustic source depths (30 and 60 m).

As already noted for temperature and salinity, the largest differences between the available operational CMEMS ocean estimates and the dedicated modelling exercises are seen in the modelled variability. An assessment of the relative performances between Exp-DD and Exp-DA based on the sound speed vertical derivative statistics is difficult; however, these small differences may be non-linearly amplified by the acoustic simulations and thus, may become relevant for assessing acoustic performance.

To qualitatively evaluate model performance, horizontal maps of daily averaged temperature at 35 m depth, similar to the fields shown in Fig. 5, are shown in Fig. 8. All the models reproduce the observed advective dynamics with warm waters entering the area of the experiment from the north-west. The CMEMS results are generally characterized by weaker horizontal temperature gradients and the error in the front location is evident. Thus, we can argue that the major differences between CMEMS products and Exp-DD or Exp-DA are not due to the temporal resolution (given that they are all daily averages in Fig. 8) but can be attributed to the lower spatial resolution of CMEMS compared to the other model implementations. CMEMS simulated temperatures are lower than the observations in the north-west sector of the experimental area and significantly higher in the remaining portion of the domain where most of the data were collected (explaining the observed warm bias). The advective process from CMEMS is less energetic with a

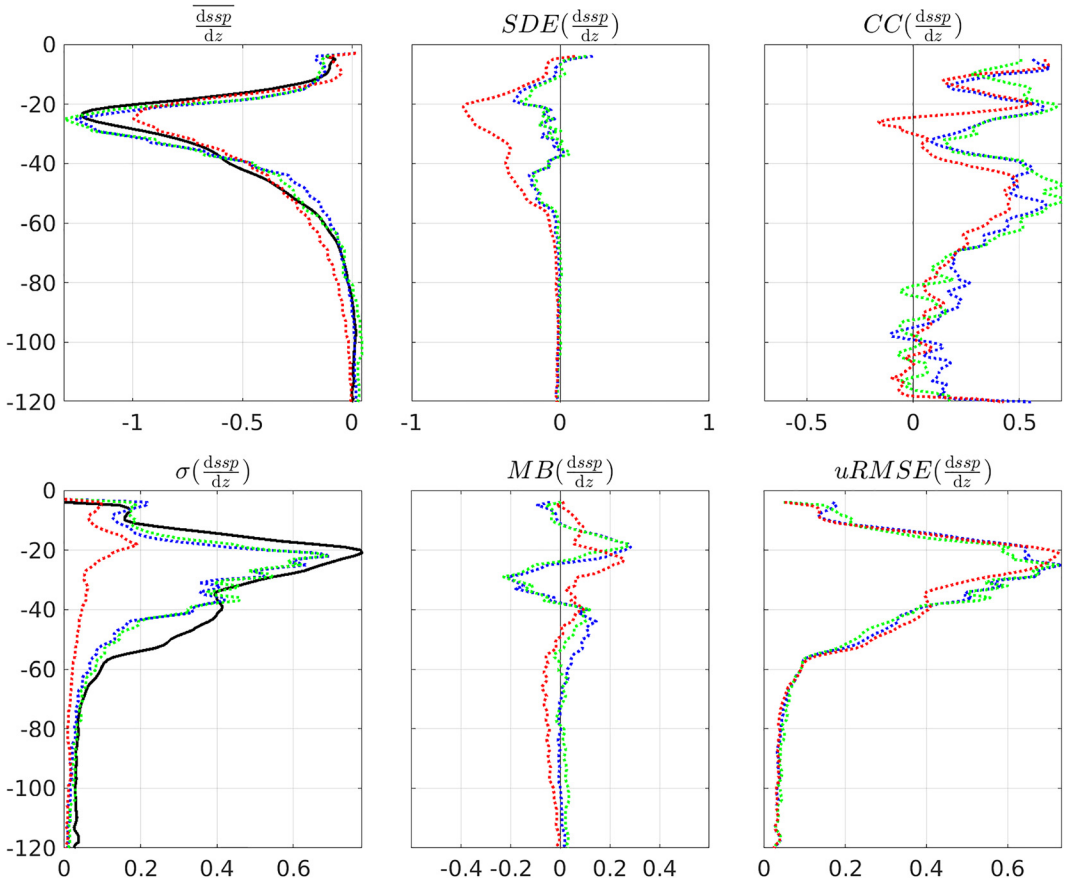

FIG. 7. (Color online) Error statistics between three different model results and available observations. Top row, from left to right: average sound speed vertical gradient (s), sound speed gradient standard deviation error (SDE), and sound speed gradient correlation coefficient (CC). Bottom panels, from left to right: sound speed gradient standard deviation (m), sound speed gradient mean bias (MB) error (m/s), and sound speed gradient unbiased root mean squared error (uRMSE). Colors as per Fig. 6. Black lines indicate observations; blue, green, and red lines are for Exp-DD, Exp-DA, and CMEMS, respectively.

reduced water mass displacement during the analyzed period; the warm waters do not reach the OM-2 location.

In contrast, Exp-DD and Exp-DA have similar temperature patterns. Due to the fine tuning for this specific MREA exercise, the horizontal temperature gradients are quite strong and comparable to the observed values (Fig. 5). The warm water mass approaching from northwest is in good agreement with the observations. The major differences between Exp-DD and Exp-DA are the location and the shape of the thermal front and the intensification of the horizontal temperature gradient in the south-western sector of the domain. Thus, data assimilation using glider data can constrain the model solution by slightly shifting the intruding water mass northward, resulting in statistically better agreement with observations (Fig. 5). The similarities between Exp-DD and Exp-DA indicate that the dynamical downscaling approach allows the more relevant features and dynamics to be incorporated into the model, providing an improved estimate of the environment. In addition, the data assimilation further improves the model dynamics.

C. Acoustic assessment

To quantitatively evaluate the acoustic performance of the four different MREA procedures, we assume that the errors introduced by the acoustic propagation model approximations act independently from the sound speed profiles, so that results described in this section are indicative of the fitness-for-purpose of the MREA strategy.

Results of previous work on the same dataset (Tollefsen, 2021) highlighted ambiguity in the analysis of the transmission loss (TL) when computed from the CW transmission. Similar, preliminary analysis confirmed the unfitness of the TL for MREA assessment, even when it was computed on a portion of the LFM signal.

However, acoustic waves traveling in a shallow-water waveguide produce a set of multiple propagation paths (rays) resulting in the arrival at the receivers of successive acoustic wave-fronts. The characteristics of the multiple wave-fronts can be related to the ocean dynamics and fluctuations (Roux *et al.*, 2008; Roux *et al.*, 2011; Aulanier *et al.*, 2013). Angles, times, and intensities of the acoustic rays detected at a receiver array are useful quantities for our acoustic validation because they can be good indicators of the dynamics and characteristics of the ocean. By analyzing the simulated TL path along transects connecting the source and the SLIVA receivers, differences between the numerical experiments can be observed in the resulting geometric characteristics. An example for an acoustic station at 2 km distance from the SLIVA along the southern transect is

https://doi.org/10.1121/10.0014805

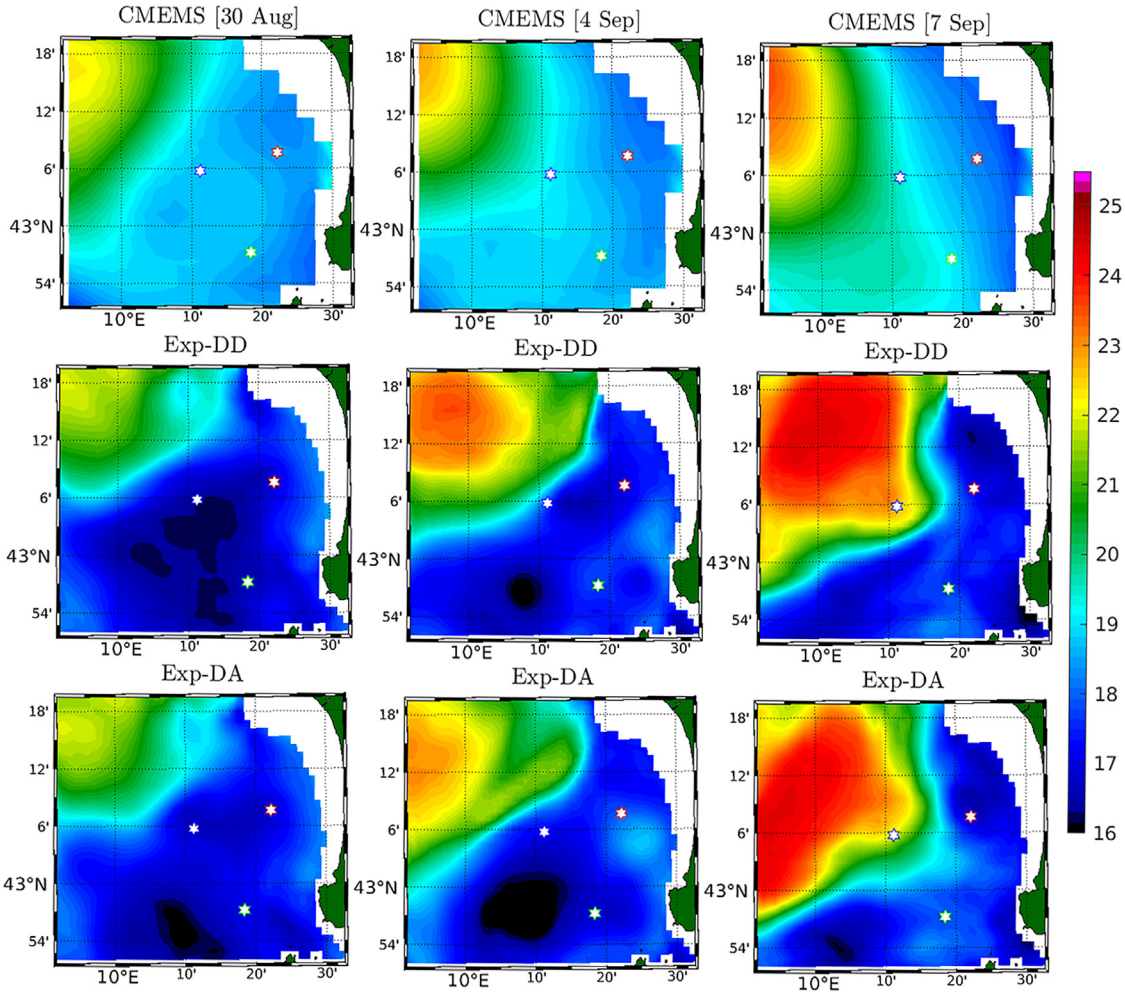

FIG. 8. (Color online) From left to right, daily averages of modelled temperature at 35 m depth valid for August 30, September 4 and 7. Top row panels are results from CMEMS operational model, middle and bottom rows are results from Exp-DD and Exp-DA, respectively. Values are in degrees Celsius. The three ocean mooring positions are also shown as stars (as in Fig. 1).

shown in Fig. 9. Even for relatively short distances between source and receivers, acoustic wave trajectories are very sensitive to the sound speed profiles resulting from the four different acoustic simulations. The different paths are characterized by a different number of surface/bottom interactions, and hence, will result in different arrival angles, arrival times and intensities at the receiver.

We extracted intensities and relative arrival times from the measured acoustic data and compared them with the corresponding quantities extracted from the four different acoustic simulations. The acoustic signals recorded by each data channel of the SLIVA receiver were filtered through a bandpass filter with 3000–3200 Hz bandwidth and cross-correlated with the transmitted LFM signal filtered at the same frequency range. To obtain a consistent quantity from the beam tracing model results, the duration of the simulated received signals was extended to match the theoretical autocorrelation peak width. A comparison between the measurements of intensity of the acoustic pressure field and the results of the acoustic simulations, using the four different sound speed profiles as input, for the station at 2 km distance from the SLIVA along the southern acoustic transect with the source at 60 m depth is shown in Fig. 10 as a function of depth and relative arrival time.

Acoustic model results were aligned with observations by matching the arrival time of the maximum peak of the observations and the Aco-CTD simulation. All the other acoustic simulations were aligned in the same fashion since they are all synchronized in the time domain. This approach worked well for the majority of the acoustic stations, with the exception of a few stations characterized by large ranges between source and receiver and thus, lower signal to noise ratio. For those specific stations, temporal alignment was performed manually.

The acoustic field in Fig. 10 is characterized by the presence of clear wave-fronts spanning the SLIVA from different angles and speckle due to interference between acoustic paths. Obviously, the model results are noise-free; however, similarities and differences between simulated and observed fields are evident in the arrival structure of the multiply reflected/refracted paths. This agreement is due in part to the relatively short range considered in this example

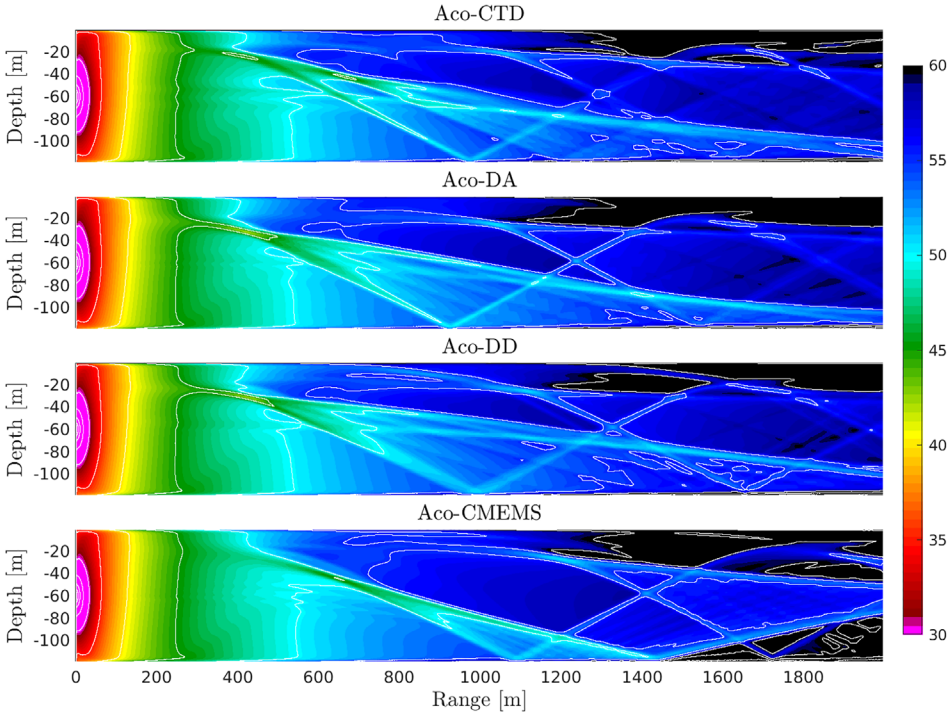

FIG. 9. (Color online) Modelled transmission loss (dB) from the acoustic source to the SLIVA. The acoustic source is deployed at 60 m depth and is located 2 km south of the receivers. White lines show contour interval of 5 dB.

(2 km). The acoustic simulation performance on the four experiments is qualitatively similar; however, only the Aco-DA, and to some degree the Aco-CMEMS, are able to reproduce the early arrival that is present in the observational field.

For a simpler physical interpretation of the comparison, or for inversion purposes (Aulanier and Nicolas, 2013), it may be useful to identify the arrivals by their reception angle on the array by performing time-delay plane wave beamforming on the received field:

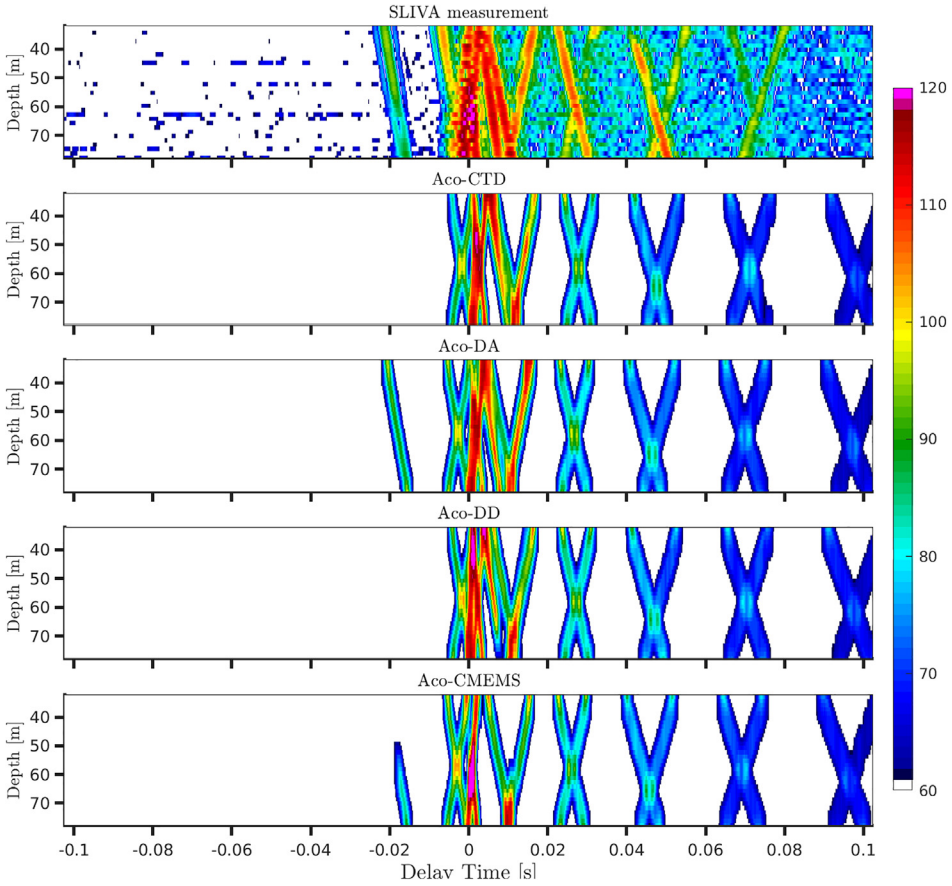

FIG. 10. (Color online) Channel impulse response at the SLIVA receiver. Y axis are depths (m), X axis are relative time (s). Colors are the sound pressure level (dB re 1 μPa). From top to bottom: observations, acoustic model results from Aco-CTD, Aco-DA, Aco-DD, and Aco-CMEMS simulations. The acoustic source is deployed at 60 m depth and is located 2 km south of the SLIVA.

https://doi.org/10.1121/10.0014805

$$I(\mathrm{t},\theta_r) = \frac{1}{N_r}\sum_{i=1}^{N_r} I(t+\tau(\theta_r,z_i),z_i), \tag{10}$$

where N_r are the 32 SLIVA channels, I is the sound intensity recorded at each channel i, and $\tau(\theta_r,z_i)$ is the delay calculated at each receiver depth (z_i).

In Fig. 11, the arrival angles of the most intense acoustic paths as a function of time (white circles with black edges) are compared with corresponding quantities predicted by the four different acoustic simulations. For the comparison in Fig. 11, we sampled the model results only at the hydrophone at the center of the simulated vertical line array. For a given time, the arrival angles for all the simulated SLIVA channels are very similar (not shown), confirming the validity of the plane wave assumption from the modelling point of view. The four different model behaviors are evident with this representation, even without using the intensity of the individual rays. Again, only the Aco-DA and Aco-CMEMS simulations predict the early arrival at –0.02 s. Furthermore, differences between the acoustic simulations are also evident in the late arrivals. In general, all the simulations predict a larger number of echoes than were actually observed, confirming that seabed attenuation properties in the acoustic model are suboptimal; however, for the purposes of the present study, we consider this fine-tuning of the model to be unnecessary.

From Figs. 10 and 11, we may argue that improved acoustic estimates may lead to significant improvements also in acoustic inversion procedures. Assimilation of acoustic data into ocean models based on acoustic tomography relies on identification and matching between predicted and observed ray arrivals and uses the arrival time differences to infer on ocean parameters. Other inversion methods, based on transmission loss (Storto *et al.*, 2021), require the linearization of the observational operator around the misfit, linearization that would strongly benefit from an improved first guess.

Even if for inversion purposes or physical interpretation, transforming the intensity data recorded from the space-time domain to the angle-time domain has clear advantages for ray identification, defining a performance matrix based on single rays and their characteristics requires multi-dimensional statistics.

Thus, we decided to compute the MSE, for each station and for each source depth, between observed and modelled intensity of the pressure field received on the SLIVA for depth and arrival time (as displayed in Fig. 10). To quantitatively compare the acoustic properties of the four different rapid environmental assessments results, we calculated the skill score (SS) of each experiment with respect to a reference experiment (Murphy, 1992):

$$\mathrm{SS} = 1 - \frac{MSE}{MSE_R}, \tag{11}$$

where the subscript R denotes a reference experiment. $\mathrm{SS} > 0$ when the considered experiment outperforms the reference experiment, $\mathrm{SS} \approx 0$ when the considered experiment and the reference experiment have similar MSE, and $\mathrm{SS} < 0$ when the considered experiment performs worse than the reference experiment.

In Fig. 12, the SS of the acoustic simulations performed using range-dependent sound speed estimates (Aco-

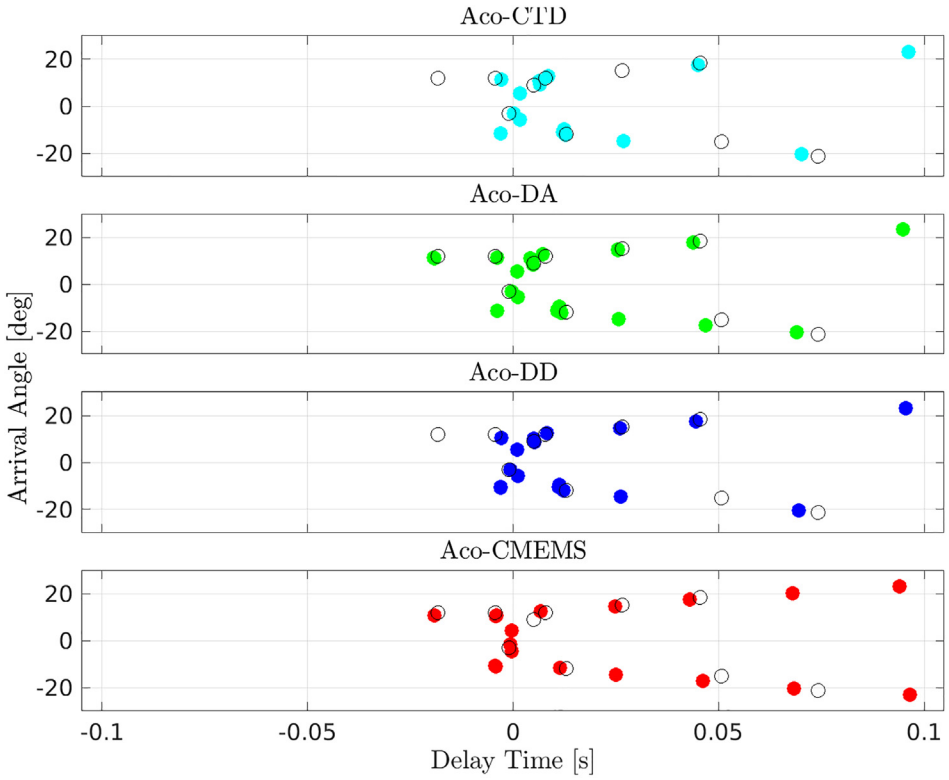

FIG. 11. (Color online) Angles versus time of arrival. White circle with black edges are the observations. The acoustic source is deployed at 60 m depth and is located 2 km south of the SLIVA.

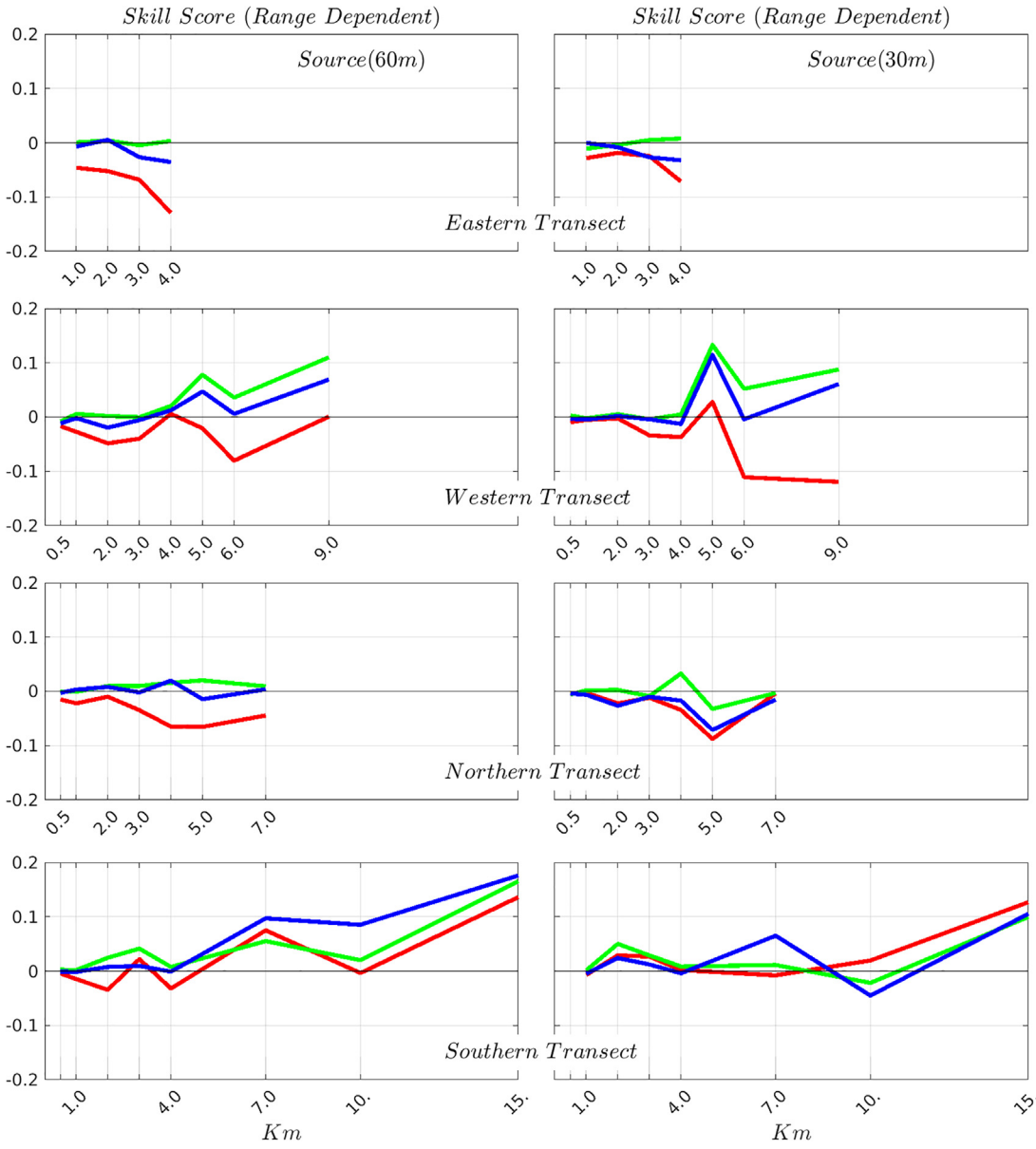

FIG. 12. (Color online) Skill Scores for Aco-CMEMS (red), Aco-DD (blue), and Aco-DA (green) acoustic simulations, using as reference the Aco-CTD results. Left column and right column indicate results for source deployed at 60 and 30 m depth, respectively. X axis in each panel indicate the station-receiver distance.

CMEMS, Aco-DD, and Aco-DA) are evaluated using the acoustic run with the measured sound speed profile at the source location (Aco-CTD) as the reference experiment. The SS are grouped by source depth (30 and 60 m) and source–receiver relative location (east, west, north, and south). Within each group, they are ordered as functions of source–receiver distances.

We consider $|SS| \leq 0.01$ (1% difference between the two MSEs) as no skill, $SS > 0.01$ as positive skill, and $SS < 0.01$ as negative skill.

When the source is deployed at 60 m depth (Fig. 12, left column), the Aco-DA experiment outperforms Aco-CTD at 41% (11 out of 27) of the acoustic stations considered, while for the remaining 16 stations (59%), the Aco-DA MSEs are similar to the Aco-CTD MSEs (SS $\approx$ 0). The Aco-DD SS is positive at 7 stations (26%), negative at 5 stations (19%), and close to 0 at 15 stations (55%). Finally, Aco-CMEMS SS is negative at 19 stations (70%), 0 at 5 stations (19%), and positive at only 3 stations (11%). The SS for Aco-DA and Aco-DD are comparable (less than 1% difference) at 14 stations out of 27, while Aco-DD outperforms Aco-DA at only 2 stations.

Statistics are slightly different when comparing data collected with the source deployed at 30 m depth with the corresponding numerical experiments. The SS for Aco-DA is positive at 8 stations (31%), 0 at 15 stations (58%), and negative at 3 stations (11%). The simple dynamical downscaling derived sound speed profiles (Aco-DD) have positive SS at 23% of the stations (6 of 26), 0 SS at 11 stations (42%), and negative SS at 9 stations ($\sim$35%). The Aco-

https://doi.org/10.1121/10.0014805

CMEMS experiment has positive SS at five stations (19%), zero SS at nine stations, and negative skill at 12 stations (46%).

Overall, considering both source depths, in the 53 separate acoustic configurations considered, the range dependent sound speed profiles extracted from the assimilative runs (Aco-DA) outperform the simple dynamical downscaling derived sound speed 24 times (45%). Aco-DD performs better than the assimilative runs (Aco-DA) at only five stations. In all the remaining configurations, they have comparable acoustic skills. The Aco-CMEMS simulations have the lowest SS, thus performing statistically worse than the Aco-DD or Aco-DA simulations. The full modelling suite, which assimilates glider data near the experimental area (Exp-DA), provides sound speed propagation estimates that are comparable or even better than the simple CTD cast derived sound speed in 50 out of the 53 acoustic configurations considered.

For relatively short acoustic ranges, when the distance between source and receiver is less than 4 km, the differences between Aco-DA, Aco-DD, and Aco-CTD tend to be small. To better understand the effects of varying the sound speed profiles along the acoustic propagation path, we computed the SS for acoustic simulations performed using range dependent sound speed profiles. The reference MSE for this calculation of SS was the MSE calculated using the results of the corresponding range independent runs (i.e., sound speed profile averaged along the acoustic transect). Thus, a positive SS indicates that including the spatial variability of the sound speed along the propagation path increases the

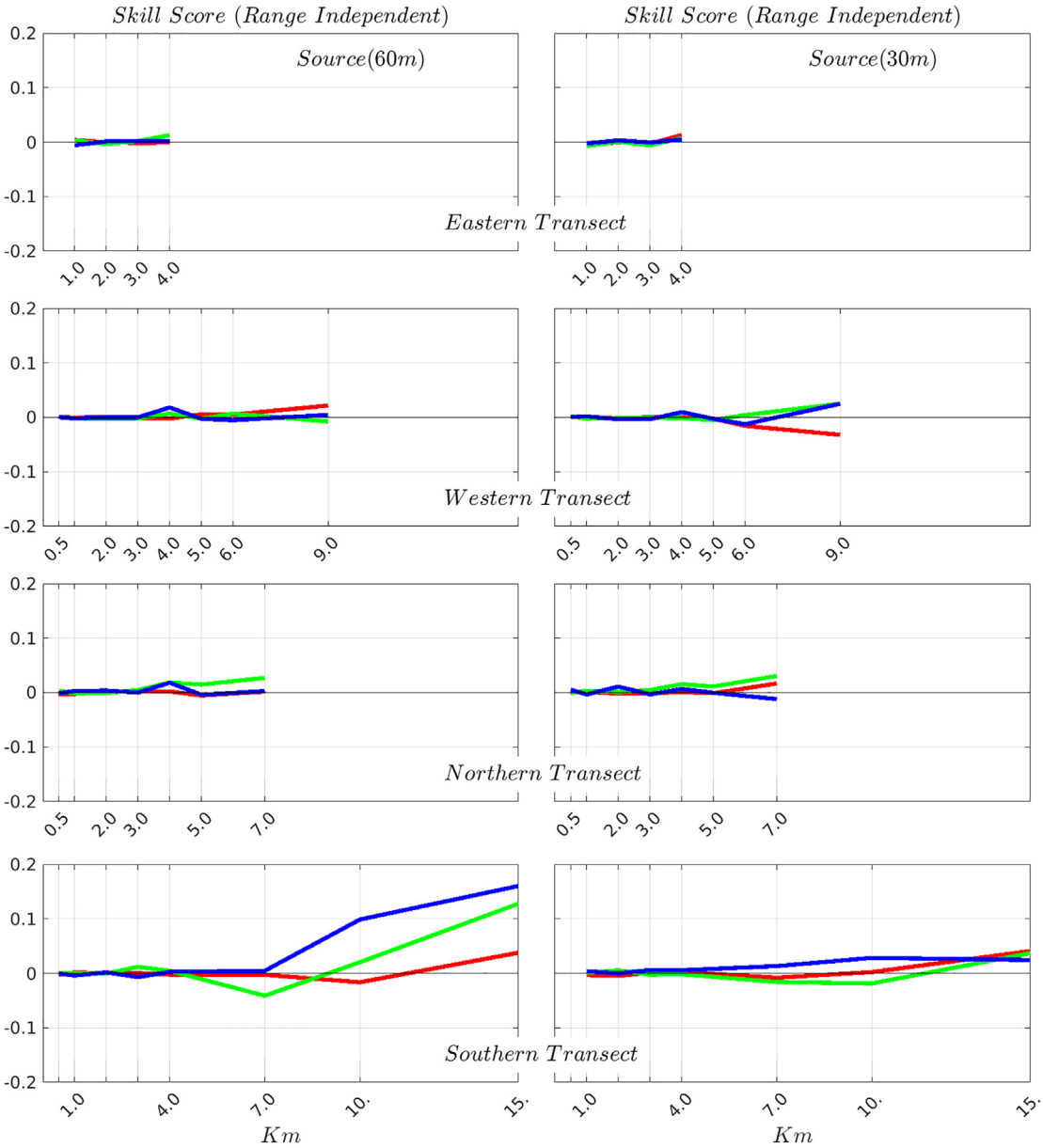

FIG. 13. (Color online) Skill Scores for Aco-CMEMS (red), Aco-DD (blue), and Aco-DA (green) range-dependent acoustic simulations, using as reference the corresponding range independent simulation results (Aco-CMEMS-RI, Aco-DD-RI, and Aco-DA-RI, respectively). Left column and right columns indicate results for source deployed at 60 and 30 m depth, respectively. X axis in each panel indicate the station-receiver distance.

skill of the model. On the other hand, a negative SS indicates the acoustic prediction is degraded by the horizontal structures predicted by the three different MREA methodologies. In the majority of the acoustic simulations performed, using an averaged range independent sound speed profile has a minor impact on the SS (Fig. 13). Considering all the MREA strategies and both the source depths, the SS is close to zero for 79% of the stations. However, the three different experiments have different statistics. Consistent with the damped spatial variability already observed, acoustic simulations performed using CMEMS derived products (Aco-CMEMS) are less sensitive to spatially varying sound speed than the other simulations.

Only 15% of the Aco-CMEMS-RI simulations have nonzero SS, confirming the previous findings that the horizontal resolution of the CMEMS products is inadequate for the scales considered in these acoustic applications. Acoustic simulations performed with sound speed estimates from the assimilative runs (Aco-DA-RI) are more sensitive to the spatial variability than equivalent simulation forced using the sound speed from the simple dynamical downscaling approach (Aco-DD-RI). Aco-DA-RI is nonzero for 28% of the considered geometries, while Aco-DD-RI is nonzero for only 21% of the simulations. Regardless, the depth of the acoustic source, differences between range dependent and range independent sound speed estimates become most relevant for ranges longer than 4 km.

There are only two stations where differences between range varying and averaged sound speed profiles produce different SS for distances shorter than 4 km. First, along the northern acoustic transect at 2 km source–receiver distance and 30 m source depth, the Aco-DD SS is positive. Second, along the southern acoustic transect at 3 km source–receiver distance and 60 m source depth, the Aco-DA SS is positive. In both of these cases, the introduction of range-dependent sound speed profiles improved the acoustic results. Considering only the acoustic geometries sensitive to the sound speed spatial variability for each experiment (i.e., ranges greater than 4 km), the Aco-CMEMS has positive SS in 60% of the stations, while both Aco-DA and Aco-DD have positive values in 80% of the considered cases. These statistics suggest that the dedicated model exercise with high horizontal resolution has skill at ranges equal or longer than 4 km. These findings agree with the ratio 10 between model resolution and effective resolution (Roache, 1998) but they could also be a consequence of the oceanographic dynamics of the area. Table III summarizes all the computed SS.

TABLE III. Summary of experiments Skill Scores. The three numbers in each cell indicate number of stations with positive, negative, and no-skill, respectively.

	Transect				
Experiment	Eastern	Western	Northern	Southern	Total
Aco-CMEMS	0-8-0	1-10-5	0-10-4	7-3-5	8-31-14
Aco-DD	0-4-4	5-3-8	1-6-7	7-1-7	13-14-26
Aco-DA	0-1-7	7-0-9	3-1-10	9-1-5	19-3-31
Aco-CMEMS-RI	1-0-7	1-2-13	1-0-13	2-1-12	5-3-45
Aco-DD-RI	0-0-8	2-1-13	2-1-11	5-0-10	9-2-42
Aco-DA-RI	1-0-7	1-0-15	6-0-8	4-3-8	12-3-38

IV. SUMMARY AND CONCLUSIONS

Obtaining an underwater sound speed estimate adequate for most acoustic applications is a challenging task for any MREA procedure. Difficulties arise from uncertainties on slowly varying environmental parameters (i.e., the sea floor geometry or the bottom acoustic properties), and from the strong nonlinear relationship between sound propagation path and the vertical shear of ocean temperature and salinity or surface properties.

Despite the existence of ocean monitoring programs, often complemented with dedicated environmental/geophysical surveys in areas of interest, significant observational gaps still remain especially for acoustic quantities, which are rarely monitored. To fill the observational gap and to produce consistent analysis and predictions of the temporal and spatial evolution of the environment, ocean observing and prediction systems, which integrate observations through assimilative ocean models, are used in MREA procedures. Assimilated data (usually temperature, salinity, sea surface elevation, or, in the most advanced systems, ocean currents) are often used to assess and validate MREA performance. Consequently, the quality of an MREA procedure in reproducing or predicting dynamics or phenomena not directly observed (like the acoustic propagation, pollutant or body dispersion) must be inferred.

In this study, we validated and assessed state-of-the-art algorithms in assimilative ocean modelling used to characterize and predict the marine environment with a specific focus on acoustic applications. The numerical exercise presented here uses the data collected during the GLISTEN-15 sea trial led by the NATO CMRE, conducted from August 26, 2015 to September 9, 2015 in the Tyrrhenian Sea. The GLISTEN-15 sea trial (Fig. 1) offered the possibility to study and characterize the performance of four different MREA strategies using synoptic ocean-acoustic observations collected by gliders, moored platforms, and CTD casts.

In addition to data products available from the Copernicus Marine Service (Le Traon *et al.*, 2019), a dedicated ocean model, based on NEMO (Madec *et al.*, 2012) was implemented in the area. The modelling suite uses a two-way nesting algorithm to reach ∼450 m horizontal resolution in the experimental area, while 141 unevenly spaced levels, with partial steps (Barnier *et al.*, 2006), define the vertical dimension. Surface fluxes, iteratively computed by means of a bulk formula (Pettenuzzo *et al.*, 2010) using the atmospheric fields provided by the ECMWF, are further constrained based on the differences between satellite products (Buongiorno Nardelli *et al.*, 2013) and model predicted SST. The parent model is initialized and one-way nested

(Oddo and Pinardi, 2008) with the Copernicus Mediterranean Sea operational model (Oddo *et al.*, 2014).

A 3DVAR assimilation procedure, based on Dobricic and Pinardi (2008), was used in the MREA procedure with assimilative capabilities. The 3DVAR was chosen because its basic assumptions and characteristics perfectly match MREA requirements. Previous studies using synthetic acoustic observations (Storto *et al.*, 2020) and a similar assimilation setup suggested the importance of the ocean data assimilation step in reproducing the acoustic characteristics variability. However, these ideas need to be extensively corroborated by real experiments. In this study we evaluate the ocean 3DVAR data assimilation capability with real oceanic and acoustic observations. We coupled the data assimilation procedure with the child model allowing the two-way nesting procedure to propagate corrections into the parent model. With the ocean modelling suite, we performed two experiments: a simple dynamical downscaling (Exp-DD) and an assimilative simulation (Exp-DA). The numerical experiments were initialized approximately 3 months before the starting of the GLISTEN-15 trial to allow the dynamics resolved by the increased model resolution to develop properly.

For the purposes of the present study, we divided the collected oceanographic dataset into two sub-sets: a small set of glider data were assimilated in the ocean model, while all the remaining observations, both oceanographic and acoustic, were used only for validation purposes. Oceanographic data used for MREA validation were acquired near the acoustic measurements, while the assimilated data were acquired outside the study area near the western and northern boundaries of the experiment (Fig. 1). Finally, to validate the acoustic performance of the MREA strategies, we reproduced the fixed source–fixed receiver acoustic experiments conducted during the trial (Table I and Fig. 1) with a range dependent ray-tracing acoustic model (Porter and Bucker, 1987; Porter and Liu, 1994) using the three different ocean simulations (CMEMS, Exp-DD, Exp-DA) as well as the CTD casts.

Analysis of oceanographic data recorded by the different platforms indicates that most of the observed variability, confined in the mixed layer temperature and MLD, is driven by advective processes (Figs. 4 and 5). A comparison between the observed CTD and available historical data are consistent with the warming and salinification processes occurring in the Mediterranean Sea in recent decades (e.g., Schroeder *et al.*, 2017).

A comparison with independent data (Fig. 6) indicates a progressive improvement from the CMEMS product to the dynamical downscaling, to the assimilative model. The largest improvements deriving from the dedicated modelling exercises (both Exp-DD and Exp-DA), in terms of temperature and salinity, are confined in the thermocline and they are evident in terms of MB and SDE. One of the major issues associated with the available CMEMS products is the underestimation of the ocean variability. It is evident that downscaling and data assimilation significantly improved model performance, due to the ability of the model to properly resolve the dominant ocean scales (Exp-DD and Exp-DA) and to accurately constrain the model solution (Exp-DA) spatially and temporally. The dynamics and variability observed are typical of summer conditions in large areas of the Mediterranean Sea, or more generally of mid-latitude oceans. We could argue that the improvements resulting from dynamic downscaling and data assimilation may be of general interest for applications in other areas of the world ocean characterized by similar dynamics. Conversely, given the great seasonal variability that characterizes MLD and associated dynamics, dedicated experiments are necessary to extend the obtained results to other seasons.

With our primary interest in underwater acoustics, an analysis of model performance in terms of the vertical sound speed gradient was also performed (Fig. 7). As with temperature and salinity, we statistically compared the vertical derivative of the sound speed, computed from the non-assimilated gliders, and from the three different ocean models. The analysis highlighted that both the dynamical downscaling and the assimilative ocean model runs improve the representation of the vertical sound speed gradient in terms of standard deviation error when compared with the CMEMS model. However, the differences between Exp-DA and Exp-DD vertical sound speed gradient statistics are relatively small and a clear acoustic assessment based on oceanographic observations is inconclusive.

From a qualitative point of view, all the ocean estimates considered (CMEMS, Exp-DD, and Exp-DA) reproduce the observed advective dynamics (Fig. 8) with warm waters entering the area of the experiment from north-west. However, the CMEMS results are generally characterized by weaker horizontal temperature gradients and dynamics, probably due to the lower resolution compared to the other model implementations. This suggests that the relatively low variability observed in the CMEMS products is mostly spatial. The comparison between Exp-DD and Exp-DA indicates that the data assimilation procedure is properly correcting the model error without affecting the model dynamics (Fig. 8).

A dedicated acoustic assessment was performed by taking advantage of the available synoptic acoustic measurements. A preliminary analysis in terms of transmission loss revealed that quantitative and robust model assessment is hard to achieve given the relatively small differences between the three different acoustic model simulations results, and the uncertainties associated with the required input variables (i.e., source level, or the spatial variability of the bottom composition, Holland and Osler, 2000). However, even though the TL is inadequate for model assessment at the acoustic receiver, differences among the four different MREA strategies are evident in terms of acoustic propagation depth-time arrivals along the considered transects (Fig. 9).

Thus, we focused our analysis on direction of arrival, times, and also intensities of the acoustic rays reaching the SLIVA receivers, since they integrate the acoustic

characteristics of the media along the range. For all the acoustic transects and for two source depths, we analyzed the SLIVA channel impulse response in a small portion of the LFM signal transmitted during the experiment (3000–3200 Hz bandwidth) and compared with equivalent quantities derived from the four different acoustic simulations (Fig. 10).

The acoustic assessment of the four MREA strategies was performed in terms of model Skill Score using as reference the acoustic simulations performed using the CTD measured sound speed profiles at time and location of the acoustic transmission (Fig. 12 and Table III).

We found that sound speed profiles extracted from the CMEMS products generate acoustic predictions skill statistically worse than the other sound speed profile estimates. Regardless of the depth of the acoustic source, Aco-DA is the best performing MREA strategy. With the acoustic source deployed at 60 m depth, at all the acoustic stations, the sound speed profiles extracted from the assimilative runs provide acoustic results equaling or exceeding in skill those modelled with the sound speed extracted from the CTD cast. With the acoustic source deployed at 30 m depth, Aco-DA outperforms Aco-CTD at all but 3 stations. However, even the relatively simple dynamical downscaling methodology (Aco-DD) results in significant improvement in skill when compared with available CMEMS products and performs comparably to the assimilative run (Aco-DA).

Despite the fact that CMEMS predictions are inadequate for acoustic predictions in the study area, the operational service provides a fundamental basis for the MREA exercises. An investigation of the relevance of sound speed profile horizontal variability (Fig. 13 and Table III) confirmed that available CMEMS products have inadequate horizontal resolution for the scales considered in these acoustic applications. On the other hand, acoustic statistics suggest that a model with high horizontal resolution and data assimilation can capture ocean structures more correctly with scales longer than approximately 4 km. In the absence of acoustic observations, we suggest that MREA procedures targeted to acoustics applications be assessed against the sound speed vertical gradient to better estimate acoustic performance. However, we have seen that only explicit acoustic simulations and the availability of acoustic observations can provide truly robust model validation. On the other hand, given that shallow water acoustic propagation is strongly sensitive to the vertical gradients of sound speed, short to medium range acoustic transmissions can provide further and more robust tests of the vertical temperature (or sound speed) structure of ocean state estimates. Finally, the good agreement of the acoustic data with the MREA results deriving from the dynamical downscaling with and without the data assimilation indicates that numerical ocean models have now reached a useful level of accuracy in the prediction of the horizontal and vertical structure of small scale oceanographic features. Thus, acoustic data can now provide useful additional constraints for ocean state estimation using classical or novel data assimilation algorithms (Storto *et al.*, 2021) to project acoustic observables into ocean state variables. The improved sound speed estimates may reduce the intrinsic difficulties in the ray identification (Mauuary, 1995; Martin-Lauzer *et al.*, 1994) in the classical ocean-acoustic tomography (Cornuelle *et al.*, 2008), or extend the validity of the linear assumption in variational inversion methods (Storto *et al.*, 2021).

ACKNOWLEDGMENTS

This work and the GLISTEN15 experiment were supported by the project "Sensing and predicting underwater noise using robotic platforms and forecast models for Maritime ISR" funded by the NATO Allied Command Transformation (ACT). Defence Research and Development Canada support was provided under the Command Reconnaissance Area Control and Coordination Environmental Network (CRACCEN) project.

Aulanier, F., and Nicolas, B. (**2013**). "Time-angle ocean acoustic tomography using sensitivity kernels: Numerical and experimental inversion results," J. Acoust. Soc. Am. **133**, 3444.

Aulanier, F., Nicolas, B., Roux, P., and Mars, J. I. (**2013**). "Time-angle sensitivity kernels for sound-speed perturbations in a shallow ocean," J. Acoust. Soc. Am. **134**, 88–96.

Barnier, B., Madec, G., Penduff, T., Molines, J.-M., Treguier, A.-M., Le Sommer, J., Beckmann, A., Biastoch, A., Böning, C., Dengg, J., Derval, C., Durand, E., Gulev, S., Remy, E., Talandier, C., Theetten, S., Maltrud, M., McClean, J., and De Cuevas, B. (**2006**). "Impact of partial steps and momentum advection schemes in a global ocean circulation model at eddy-permitting resolution," Ocean Dyn. **56**, 543–567.

Borrione, I., Oddo, P., Russo, A., and Coelho, E. (**2019**). "Understanding altimetry signals in the Northeastern Ligurian Sea using a multi-platform approach," Deep Sea Res. Part I: Oceanogr. Res. **145**, 83–96.

Bosse, A., Testor, P., Mortier, L., Prieur, L., Taillandier, V., d'Ortenzio, F., and Coppola, L. (**2015**). "Spreading of Levantine Intermediate Waters by submesoscale coherent vortices in the northwestern Mediterranean Sea as observed with gliders," J. Geophys. Res. Oceans **120**(3), 1599–1622.

Boyer, T. P., Baranova, O. K., Coleman, C., Garcia, H. E., Grodsky, A., Locarnini, R. A., Mishonov, A. V., Paver, C. R., Reagan, J. R., Seidov, D., Smolyar, I. V., Weathers, K., and Zweng, M. M. (**2018**). in *World Ocean Database 2018*, edited by A. V. Mishonov, NOAA Atlas NESDIS 87.

Buongiorno Nardelli, B., Tronconi, C., Pisano, A., and Santoleri, R. (**2013**). "High and Ultra-High resolution processing of satellite Sea Surface Temperature data over Southern European Seas in the framework of MyOcean project," Remote Sens. Environ. **129**, 1–16.

Cornuelle, B. D., Worcester, P. F., and Dzieciuch, M. A. (**2008**). "Ocean acoustic tomography," J. Phys.: Conf. Ser. **118**, 012002.

Debreu, L., Vouland, C., and Blayo, E. (**2008**). "AGRIF: Adaptive Grid Refinement in Fortran," Comput. Geosci. **34**(1), 8–13.

Dobricic, S., and Pinardi, N. (**2008**). "An oceanographic three-dimensional assimilation scheme," Ocean Model. **22**, 89–105.

Etter, P. C. (**2012**). "Advanced application for underwater acoustic modeling," Adv. Acoust. Vib. **2012**, 1–28.

Flather, R. A. (**1976**). "A tidal model of the northwest European continental shelf," Mem. Soc. R. Sci. Lieges **6**, 141–164.

Gandin, L. (**1963**). "Objective analysis of meteorological fields," in *Leningrad: Gridromet, English Translation 1965* (Israel Program for Scientific Translation, Jerusalem), 242 pp.

Jacobs, G., D'Addezio, J. M., Ngodock, H., and Souopgui, I. (**2021**). "Observation and model resolution implications to ocean prediction," Ocean Modell. **159**, 101760.

Hagen, P. E., Størkersen, N., Marthinsen, B.-E., Sten, G., and Vestgård, K. (**2008**). "Rapid environmental assessment with autonomous underwater vehicles—examples from HUGIN operations," J. Mar. Syst. **69**, 137–145.

Helber, R. W., Barron, C. N., Carnes, M. R., and Zingarelli, R. A. (**2008**). "Evaluating the sonic layer depth relative to the mixed layer depth," J. Geophys. Res. **113**, C07033, https://doi.org/10.1029/2007JC004595

Holland, C. W., and Osler, J. (**2000**). "High-resolution geoacoustic inversion in shallow water: A joint time- and frequency domain technique," J. Acoust. Soc. Am. **107**(3), 1263–1279.

Jensen, F., Kuperman, W., Porter, M., and Schmidt, H. (**1994**). "Computational ocean acoustics," in *AIP Series in Modern Acoustics and Signal Processing* (Springer, New York).

Legler, D. M., Freeland, H. J., Lumpkin, R., Ball, G., McPhaden, M. J., North, S., Crowley, R., Goni, G. J., Send, U., and Merrifield, M. A. (**2015**). "The current status of the real-time in situ Global Ocean Observing System for operational oceanography," J. Oper. Oceanogr. **8**(2), s189–s200.

Lengaigne, M., Menkes, C., Aumont, O., Gorgues, T., Bopp, L., André, J.-M., and Madec, G. (**2007**). "Influence of the oceanic biology on the tropical pacific climate in a coupled general circulation model," Clim. Dyn. **28**(5), 503–516.

Lermusiaux, P. F. J., and Robinson, A. R. (**2001**). "Features of dominant mesoscale variability, circulation patterns and dynamics in the Strait of Sicily," Deep-Sea Res. I **48**(9), 1953–1997.

Le Traon, P. Y., Antoine, D., Bentamy, A., Bonekamp, H., Breivik, L. A., Chapron, B., Corlett, G., Dibarboure, G., DiGiacomo, P., Donlon, C., Faugère, Y., Font, J., Girard-Ardhuin, F., Gohin, F., Johannessen, J. A., Kamachi, M., Lagerloef, G., Lambin, J., Larnicol, G., Le Borgne, P., Leuliette, E., Lindstrom, E., Martin, M. J., Maturi, E., Miller, L., Mingsen, L., Morrow, R., Reul, N., Rio, M. H., Roquet, H., Santoleri, R., and Wilkin, J. (**2015**). "Use of satellite observations for operational oceanography: Recent achievements and future prospects," J. Oper. Oceanogr. **8**(sup1), s12–s27.

Le Traon, P. Y., Reppucci, A., Alvarez Fanjul, E., Aouf, L., Behrens, A., Belmonte, M., Bentamy, A., Bertino, L., Brando, V. E., Kreiner, M. B., Benkiran, M., Carval, T., Ciliberti, S. A., Claustre, H., Clementi, E., Coppini, G., Cossarini, G., De Alfonso Alonso-Muñoyerro, M., Delamarche, A., Dibarboure, G., Dinessen, F., Drevillon, M., Drillet, Y., Faugere, Y., Fernández, V., Fleming, A., Garcia-Hermosa, M. I., Sotillo, M. G., Garric, G., Gasparin, F., Giordan, C., Gehlen, M., Gregoire, M. L., Guinehut, S., Hamon, M., Harris, C., Hernandez, F., Hinkler, J. B., Hoyer, J., Karvonen, J., Kay, S., King, R., Lavergne, T., Lemieux-Dudon, B., Lima, L., Mao, C., Martin, M. J., Masina, S., Melet, A., Buongiorno Nardelli, B., Nolan, G., Pascual, A., Pistoia, J., Palazov, A., Piolle, J. F., Pujol, M. I., Pequignet, A. C., Peneva, E., Pérez Gómez, B., Petit de la Villeon, L., Pinardi, N., Pisano, A., Pouliquen, S., Reid, R., Remy, E., Santoleri, R., Siddorn, J., She, J., Staneva, J., Stoffelen, A., Tonani, M., Vandenbulcke, L., von Schuckmann, K., Volpe, G., Wettre, C., and Zacharioudaki, A. (**2019**). "From observation to information and users: The Copernicus Marine Service Perspective," Front. Mar. Sci. **6**, 234–256.

Madec, G., and the NEMO team (**2012**). "NEMO ocean engine," in *Note du Pole de Modélisation (Note from the Modeling Pole)* (Institut Pierre-Simon Laplace, Paris, France), 1288–1619.

Martin-Lauzer, F. R., Mauuary, D., and Stephan, Y. (**1994**). "Probabilistic ray identification: A new tool for ocean acoustic tomography," in *Proceedings of ICASSP '94. IEEE International Conference on Acoustics, Speech and Signal Processing*, Vol. 2, pp. II/305-II/308.

Mauuary, D. (**1995**). "Ray identification theory in ocean acoustic tomography," J. Acoust. Soc. Am. **97**, 3235.

Murphy, A. H. (**1992**). "Climatology, persistence, and their linear combination as standards of reference in skill scores," Weather Forecast. **7**, 692–698.

Oddo, P., Bonaduce, A., Pinardi, N., and Guarnieri, A. (**2014**). "Sensitivity of the Mediterranean Sea level to atmospheric pressure and free surface elevation numerical formulation in NEMO," Geosci. Model Dev. **7**, 3001–3015.

Oddo, P., and Pinardi, N. (**2008**). "Lateral open boundary conditions for nested limited area models: A scale selective approach," Ocean Model. **20**, 134–156.

Oddo, P., Storto, A., Dobricic, S., Russo, A., Lewis, C., Onken, R., and Coelho, E. (**2016**). "A hybrid variational-ensemble data assimilation scheme with systematic error correction for limited-area ocean models," Ocean Sci. **12**, 1137–1153.

Oke, P. R., Allen, J. S., Miller, R. N., Egbert, G. D., Austin, J. A., Barth, J. A., Boyd, T. J., Kosro, P. M., and Levine, M. D. (**2002**). "A modeling study of the three-dimensional continental shelf circulation off Oregon. Part I: Model-data comparison," J. Phys. Oceanogr. **32**, 1360–1382.

Pettenuzzo, D., Large, W. G., and Pinardi, N. (**2010**). "On the corrections of ERA-40 surface flux products consistent with the Mediterranean heat and water budgets and the connection between basin surface total heat flux and NAO," J. Geophys. Res. **115**, C06022, https://doi.org/10.1029/2009JC005631.

Porter, M. B., and Bucker, H. P. (**1987**). "Gaussian beam tracing for computing ocean acoustic fields," J. Acoust. Soc. Am. **82**, 1349–1359.

Porter, M. B., and Liu, Y. C. (**1994**). "Finite-element ray tracing," in *Theoretical and Computational Acoustics*, edited by D. Lee and M. H. Schultz (World Scientific Publishing, Singapore), Vol. 2, pp. 947–956.

Roache, P. J. (**1998**). *Fundamentals of Computational Fluid Dynamics* (Hermosa, Albuquerque).

Robinson, A. R., and Golnaraghi, M. (**1994**). "The physical and dynamical oceanography of the mediterranean sea," in *Ocean Processes in Climate Dynamics: Global and Mediterranean Examples. NATO ASI Series*, Vol. 419, edited by P. Malanotte-Rizzoli and A. R. Robinson (Springer, Dordrecht).

Robinson, A. R., and Sellschopp, J. (**2002**). "Rapid assessment of the coastal ocean environment," in *Ocean Forecasting: Conceptual Basis and Applications*, edited by N. Pinardi and J. Woods (Springer-Verlag, New York), pp. 199–229.

Roux, P., Cornuelle, B. D., Kuperman, W. A., and Hodgkiss, W. S. (**2008**). "The structure of raylike arrivals in a shallow-water waveguide," J. Acoust. Soc. Am. **124**, 3430–3439.

Roux, P., Iturbe, I., Nicolas, B., Virieux, J., and Mars, J. I. (**2011**). "Travel-time tomography in shallow water: Experimental demonstration at an ultrasonic scale," J. Acoust. Soc. Am. **130**(3), 1232–1241.

Schroeder, K., Chiggiato, J., Josey, S. A., Borghini, M., and Sparnocchia, S. (**2017**). "Rapid response to climate change in a marginal sea," Sci. Rep. **7**, 4065.

Shchepetkin, A. F., and McWilliams, J. C. (**2005**). "The regional oceanic modeling system (ROMS): A split-explicit, free-surface, topography-following-coordinate ocean model," Ocean Modell. **9**(4), 347–404.

Signell, R. P., Carniel, S., Chiggiato, J., Janecovic, I., Pullen, J., and Sherwood, C. (**2008**). "Collaboration tools and techniques for large model datasets," J. Mar. Syst. **65**, 154–161.

Storto, A., De Magistris, G., Falchetti, S., and Oddo, P. (**2021**). "A neural network–based observation operator for coupled ocean–acoustic variational data assimilation," Mon. Weather Rev. **149**(6), 1967–1985.

Storto, A., Falchetti, S., Oddo, P., Yong-Min Jiang, Y.-M., and Tesei, A. (**2020**). "Assessing the impact of different ocean analysis schemes on oceanic and underwater acoustic predictions," J. Geophys. Res. Ocean **125**, e2019JC015636, https://doi.org/10.1029/2019JC015636.

Szekely, T., Gourrion, J., Pouliquen, S., and Reverdin, G. (**2019**). "CORA, Coriolis Ocean Dataset for Reanalysis," Corpernicus (published online).

Tollefsen, C. D. S. (**2021**). "Predicting acoustic variability: Pragmatic considerations for selecting a stochastic or deterministic approach," IEEE J. Oceanic Eng. **46**(3), 1045–1056.

Umlauf, L., and Burchard, H. (**2003**). "A generic length-scale equation for geophysical turbulence models," J. Mar. Res. **61**(2), 235–265.

Umlauf, L., and Burchard, H. (**2005**). "Second-order turbulence closure models for geophysical boundary layers. A review of recent work," Continental Shelf Res. **25**(7-8), 795–827.

Weatherall, P., Marks, K. M., Jakobsson, M., Schmitt, T., Tani, S., Arndt, J. E., Rovere, M., Chayes, D., Ferrini, V., and Wigley, R. (**2015**). "A new digital bathymetric model of the world's oceans," Earth Space Sci. **2**, 331–345.

Weinberg, H., and Keenan, R. E. (**1996**). "Gaussian ray bundles for modeling high-frequency propagation loss under shallow-water conditions," J. Acoust. Soc. Am. **100**(3), 1421–1431.

Zalesak, S. T. (**1979**). "Fully multidimensional flux-corrected transport algorithms for fluids," J. Comput. Phys. **31**(3), 335–362.